BEILSTEIN JOURNAL OF NANOTECHNOLOGY

Applications of Raman spectroscopy in the characterization of nanomaterials

Edited by Paulo T. Araujo and Alexandre R. Paschoal

Imprint

Beilstein Journal of Nanotechnology
www.bjnano.org
ISSN 2190-4286
Email: journals-support@beilstein-institut.de

The *Beilstein Journal of Nanotechnology* is published by the Beilstein-Institut zur Förderung der Chemischen Wissenschaften.

Beilstein-Institut zur Förderung der Chemischen Wissenschaften
Trakehner Straße 7–9
60487 Frankfurt am Main
Germany
www.beilstein-institut.de

BEILSTEIN JOURNAL OF NANOTECHNOLOGY

Determining by Raman spectroscopy the average thickness and *N*-layer-specific surface coverages of MoS_2 thin films with domains much smaller than the laser spot size

Felipe Wasem Klein[1], Jean-Roch Huntzinger[1], Vincent Astié[2], Damien Voiry[3], Romain Parret[4], Houssine Makhlouf[1], Sandrine Juillaguet[1], Jean-Manuel Decams[2], Sylvie Contreras[1], Périne Landois[1], Ahmed-Azmi Zahab[1], Jean-Louis Sauvajol[1] and Matthieu Paillet[*1]

Full Research Paper

Open Access

Address:
[1]Laboratoire Charles Coulomb, Université de Montpellier, CNRS, F-34095, Montpellier, France, [2]Annealsys, 139 Rue des Walkyries, 34000 Montpellier, France, [3]Institut Européen des Membranes, IEM, UMR 5635, Université Montpellier, ENSCM, CNRS, Montpellier, France and [4]Aix Marseille Université, CNRS, CINAM, UMR 7325, Campus de Luminy, 13288, Marseille, France

Email:
Matthieu Paillet[*] - matthieu.paillet@umontpellier.fr

* Corresponding author

Keywords:
molybdenum disulfide; number of layers; Raman spectroscopy; thin film; transition metal dichalcogenides

Beilstein J. Nanotechnol. **2024,** *15,* 279–296.
https://doi.org/10.3762/bjnano.15.26

Received: 13 November 2023
Accepted: 20 February 2024
Published: 07 March 2024

This article is part of the thematic issue "Applications of Raman spectroscopy in the characterization of nanomaterials".

Guest Editor: P. Araujo

Abstract

Raman spectroscopy is a widely used technique to characterize nanomaterials because of its convenience, non-destructiveness, and sensitivity to materials change. The primary purpose of this work is to determine via Raman spectroscopy the average thickness of MoS_2 thin films synthesized by direct liquid injection pulsed-pressure chemical vapor deposition (DLI-PP-CVD). Such samples are constituted of nanoflakes (with a lateral size of typically 50 nm, i.e., well below the laser spot size), with possibly a distribution of thicknesses and twist angles between stacked layers. As an essential preliminary, we first reassess the applicability of different Raman criteria to determine the thicknesses (or layer number, *N*) of MoS_2 flakes from measurements performed on reference samples, namely well-characterized mechanically exfoliated or standard chemical vapor deposition MoS_2 large flakes deposited on 90 ± 6 nm SiO_2 on Si substrates. Then, we discuss the applicability of the same criteria for significantly different DLI-PP-CVD MoS_2 samples with average thicknesses ranging from sub-monolayer up to three layers. Finally, an original procedure based on the measurement of the intensity of the layer breathing modes is proposed to evaluate the surface coverage for each *N* (i.e., the ratio between the surface covered by exactly *N* layers and the total surface) in DLI-PP-CVD MoS_2 samples.

Introduction

The advent of two-dimensional (2D) layered materials beyond graphene has initiated a new field of research [1-3]. In the family of 2D layered structures, transition metal dichalcogenides (TMDs) have attracted considerable attention from academia and regarding potential applications [4-9] because of a number of remarkable properties [10-12]. Particularly, it was found that the properties of layered TMDs drastically change when their thickness is reduced to a monolayer [13,14]. Layered TMD structures have a graphite-like structure with each graphene sheet replaced with an X–M–X or MX_2 triatomic layer, where X is a chalcogen atom (e.g., sulfur, selenium, or tellurium) and M is a transition metal atom (e.g., molybdenum or tungsten) [10].

Among the layered TMD materials, molybdenum disulfide, MoS_2, is of particular interest in optoelectronic applications because of its transition to a direct bandgap semiconductor with very high photoluminescence quantum yield when thinned down to a monolayer [13-17]. Its unique electronic and optical properties could provide an edge in many future applications.

The multilayers MoS_2 structures are of the most common 2Hc type, where atomic layers are arranged in such way that the stacking between two adjacent layers corresponds to a twist angle of $\theta = 60°$, and any Mo atom is sitting on top of two S atoms of the adjacent layers [18,19]. However, during the synthesis process (e.g., chemical vapor deposition (CVD) synthesis) or when using precise transfer or AFM tip manipulation techniques [20], twisted MoS_2 can be formed with two adjacent layers stacked with a relative twist angle (θ) varying from 0 to 60°. Such twisted-layered MoS_2 structures can exhibit a variety of interesting physical properties including unconventional super conductivity [21,22], non-linear optics [23,24], and moiré excitons [25].

Because the properties of MoS_2 flakes are first a function of their thickness, or layer number (N), it is of a primary importance to determine the N of MoS_2 flakes, including twisted MoS_2 flakes and defective MoS_2 flakes, synthesized by different ways. Independently of the structural organization between adjacent layers, a MoS_2 flake is usually named NL-MoS_2, or simply NL, with N being the number of MoS_2 triatomic layers, which defines the thickness of the flake.

Several optical techniques have been developed to identify the N of MoS_2 flakes produced by different methods. Among these techniques, Raman spectroscopy is widely used thanks to its convenience, non-destructiveness, and sensitivity to materials change, including strain, temperature, doping, and defects [26]. Concerning the characterization of MoS_2 flakes, different information can be derived from the measurement of the Raman features (frequencies, linewidths, and intensities) of intralayer phonon modes as well as those of the interlayer modes, the so-called layer breathing (LB) modes and shear (S) modes.

Recently, we have developed the reproducible direct growth of wafer-scale MoS_2 thin films on SiO_2/Si substrates by direct liquid injection pulsed-pressure chemical vapor deposition (DLI-PP-CVD) using low-toxicity precursors [27]. Such MoS_2 thin films showed good stoichiometry (Mo/S = 1.94–1.95) and the potential for high photoluminescence quantum yield. However, atomic force microscopy revealed that they are constituted of nanoflakes (with a lateral size of typically 50 nm) with possibly a distribution of thicknesses. Furthermore, depending on the synthesis conditions, the MoS_2 surface coverage can be incomplete, and the thin film average thickness can vary. These samples thus have characteristics, especially thickness inhomogeneities smaller than the laser spot size, that differ from the ones used to establish Raman spectroscopy-based MoS_2 layer counting methods [26,28-33]. In this context, the primary purpose of this work is to develop and validate an approach for determining the average thickness of such sub-laser spot size inhomogeneous MoS_2 thin films using Raman spectroscopy.

First, we reassess here as a ground work the information that can be derived from the Raman spectra of MoS_2 flakes for the evaluation of their thickness, N. Different Raman criteria for the determination of the thicknesses of MoS_2 flakes are first recollected; after the specification of the experimental protocol, domains and limits of application of these criteria are precisely defined from measurements performed on reference samples. These samples are well-characterized, either mechanically exfoliated or standard CVD MoS_2 large flakes deposited on 90 ± 6 nm SiO_2 on Si substrates. Then, we determine which Raman information is relevant to estimate the average thickness of MoS_2 samples produced by the DLI-PP-CVD method, which are constituted of nanoflakes and, thus, significantly different from the reference samples. Finally, an original procedure based on the layer breathing mode intensities is proposed to evaluate the surface coverage for each N, that is, the ratio between the surface covered by exactly N layers and the total surface, in DLI-PP-CVD samples.

Results and Discussion

Experimental procedure

To define a robust experimental Raman protocol to evaluate the thickness of a MoS_2 flake (i.e., its number of layers, N), it is first necessary to specify some parameters that can have a direct influence on the quality and accuracy of the results. The first parameter is the wavelength of the incident laser light used in

the Raman experiments. As it will be detailed in the following, the measurements of the frequencies, linewidths, and intensity of first-order Raman active phonon modes of MoS_2 have to be obtained with good accuracy in order to evaluate the thickness of a MoS_2 flake. These phonons modes are (i) the in-plane phonon mode involving relative motion of Mo and S atoms with E′ symmetry for a monolayer (E^1_{2g} for bulk) and (ii) the out-of-plane phonon mode involving only out-of-plane motions of S atoms with A'_1 symmetry for a monolayer (A_{1g} for bulk). These modes are located around 385 and 405 cm^{-1}, respectively, in neutral and defect-free MoS_2 monolayers [33,34]. More precisely, in MoS_2 multilayers, the symmetries of these phonon modes are E′ and A'_1 for an odd number of layers, and E_g and A_{1g} for an even number of layers. For simplicity, hereafter when we will discuss the dependence on N of the features of these phonon modes, they will be simply referred to as in the bulk, E^1_{2g} and A_{1g}, independently of the number of layers.

A drastic change of the Raman spectra, especially in the frequency range of the A_{1g} and E^1_{2g} modes, occurs when the spectra are excited at an energy close to those of the A and B excitons located around 655 nm (1.89 eV) and 601 nm (2.06 eV), respectively, in MoS_2 monolayers [35,36]. When the incident laser energy is in the range of the A and B exciton energies (the so-called resonance conditions), other bands associated to different second-order processes are observed in the Raman spectra with a strong intensity, their frequencies, widths, and intensity depending on the excitation energy [36]. In addition, resonance conditions alter the symmetry selection rules of phonons of MoS_2 [35]. Some of the second-order bands overlap with the A_{1g} and E^1_{2g} modes, complicating the exact determination of the parameters of these modes recorded under resonance conditions. Furthermore, since the MoS_2 exciton characteristics (energy, width, and spectral weight) can be changed by several factors (e.g., stacking, strain, doping, and defects), the Raman intensities measured with a single laser wavelength close to exciton energies can be affected by external factors and differ for samples elaborated by different methods. For these reasons and in the aim to use Raman spectroscopy to count the number of MoS_2 layers, one must necessarily work under off-resonance conditions, that is, by using incident laser energy far from both exciton resonance energies. In this work, we chose to perform Raman experiments using 532 nm (2.33 eV) laser excitation, because this is sufficiently far from the energy range of A and B excitons [35].

All Raman spectra reported in this paper were recorded on different samples deposited on SiO_2/Si(100) substrate. Hence, the second parameter essential to define is the SiO_2 thickness. Indeed, the multiple reflection interferences that occur in the air/MoS_2/SiO_2/Si structure influence significantly the intensity of the phonon modes [28,37]. In this work, we chose to focus on substrates with a SiO_2 thickness around 90 nm, which corresponds to the first optimum value for MoS_2 monolayer (N = 1) Raman enhancement with a 532 nm excitation energy and also amplifies the signal in the wavelength range of photoluminescence emission (around 650 nm).

The third parameter to define is the power of the 532 nm light, P_λ, impinging the sample. Much of the Raman information available to evaluate the thickness of MoS_2 flakes is based on the following parameters: (i) on precise measurements of frequency of the A_{1g} and E^1_{2g} phonon modes of MoS_2. These lead to a precise knowledge of the frequency difference $\Delta\omega_{A-E}$. It was established that $\Delta\omega_{A-E}$ depends monotonously on the number of layers, and $\Delta\omega_{A-E}$ is largely used as criterion to evaluate the thickness of MoS_2 flakes [26,29,30]; (ii) on the precise evaluation of the integrated intensities of the phonon modes of MoS_2, namely $A(A_{1g})$ and $A(E^1_{2g})$, with respect to the integrated intensity of the 521 cm^{-1} mode from a bare area of the oxidized silicon substrate, A_0(Si), used as an intensity reference [31], or from the silicon substrate underneath the MoS_2 flake, A_{2D}(Si) [28]; (iii) on the precise measurement of the A_{2D}(Si)/A_0(Si) intensity ratio [31]; and (iv) on the measurement of ultralow-frequency modes, the so-called breathing modes and shear modes. The frequencies and the number of LB and S modes allow one to identify the number of layers [32,33] and the presence of twist between adjacent layers from the vanishing of the S modes in twisted MoS_2 flakes [20,38-41].

Then, it is essential to determine the limit value of the laser power so that the above measurements are not affected by laser irradiation. Figure 1 shows the evaluation of the temperature of MoS_2 flakes prepared in different ways and that of the Si substrate as functions of the laser power impinging on the sample through a 100× objective (N.A. 0.9). The power was cycled between ≈5 μW and ≈2 mW. The temperature of MoS_2 flakes is evaluated from the Stokes/anti-Stokes intensity ratio of A_{1g} phonon modes (similar results are obtained using E^1_{2g}) and that of silicon from the Stokes/anti-Stokes intensity ratio of the 521 cm^{-1} Si mode (see [42] for method details). While the silicon temperature is quasi-insensitive to P_λ, the temperature of MoS_2 flakes changes monotonically, reversibly, and quasi-linearly with P_λ (see inset of Figure 1). For MoS_2, we found an increase rate of 25–30 °C/mW for monolayers (1L-MoS_2) and 40–45 °C/mW for bilayers (2L-MoS_2). Usual effects of sample heating are the frequency shift of the phonon modes and their concomitant broadening. In Supporting Information File 1, the frequency and the linewidth of the Si mode as functions of the laser power are displayed (Figure S2). These two parameters are found to be insensitive to P_λ below 0.5 mW. More intriguing is the evolution of the frequency (Figure 2a) and width (Figure 2b)

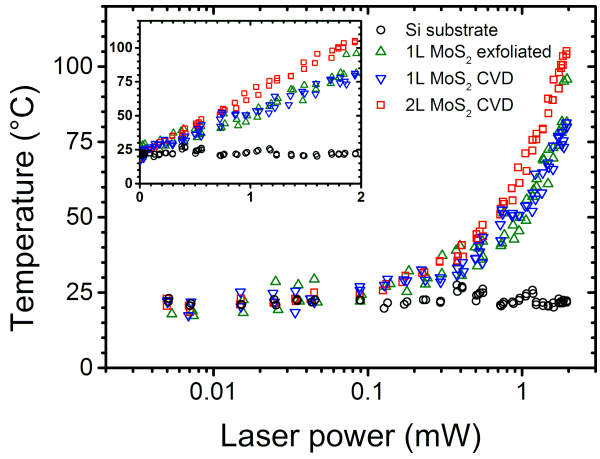

Figure 1: Evolution of the temperature of Si substrate (black circles) and MoS_2 flakes (1L exfoliated: green upward triangles, 1L CVD: blue downward triangles, and 2L CVD: red squares) as functions of the incident laser power in log-scale. The absolute values of the temperature under the laser spot were measured from the variation of the Stokes/AntiStokes ratio of the 521 cm^{-1} Si mode for the substrate and of the A_{1g} phonon modes for MoS_2 flakes. Inset, same data plotted with a linear laser power scale.

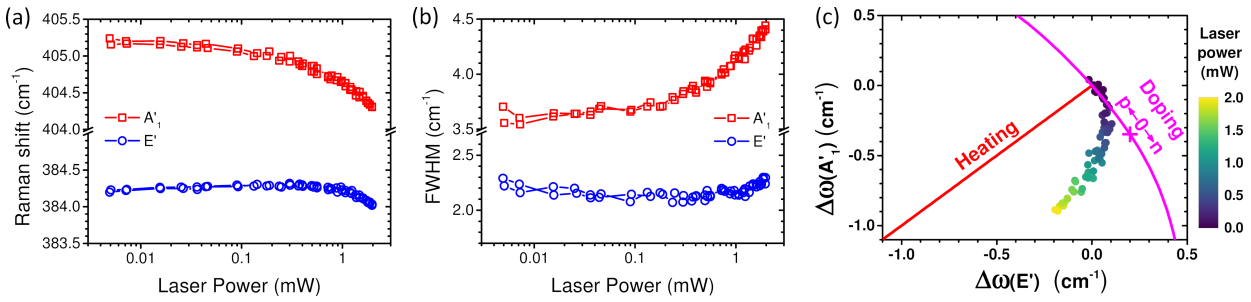

Figure 2: CVD 1L-MoS_2. Evolution of A'_1 (red squares) and E′ (blue circles) Raman modes frequencies (a) and full width at half maximum (b) as functions of the incident laser power during a cycle from 5 μW up to 2 mW and back to 5 μW. (c) Evolution of the A'_1 relative shift versus the E′ relative shift as a function of laser power. The color code of each point corresponds to the incident laser power as displayed on the color bar. The data are compared to the expected evolutions for heating effect only [43] (red line) and for doping only [44] (magenta line). To enable direct comparison, the strain contribution has been removed, and the corresponding zero doping point is labeled as well as the directions corresponding to *p* and *n* doping.

of the phonon modes of 1L-MoS_2 as a function of P_λ. For a simple thermal effect [43] and given the 25–30 °C/mW temperature increase rate determined previously, the frequencies of A'_1 and E′ modes should both downshift by 0.3–0.4 cm^{-1}/mW and the width of A'_1 should increase by ≈0.2 cm^{-1}/mW (the width of E′ should remain constant) contrary to what is observed in Figure 2a,b. To clarify this point, we present in Figure 2c (filled dots) the relative shift of the frequency of the A'_1 mode versus that of the E′ mode measured on CVD 1L-MoS_2 at different laser powers. In the same plot the expected shifts of these modes are reported (i) as functions of a pure thermal effect (Figure 2c, red line) [43] and (ii) as functions of the doping state (Figure 2c, magenta curve) [44]. Clearly the relative shift of the A'_1 mode frequency versus that of the E′ mode frequency as a function of P_λ significantly differs from the behavior expected by considering a simple thermal effect. Consequently, the results reported in Figure 2c clearly evidence photo-doping of 1L-MoS_2 concomitant with a thermal effect, as already observed for MoS_2 on SiO_2/Si [45] as well as for graphene [42]. Furthermore, the evolution of the A'_1 and E′ widths with P_λ (Figure 2b), that is, the weak change of the E′ width and the significant increase of the A'_1 width concomitant with the A'_1 frequency decrease, support this interpretation [44]. For a laser power smaller than 0.3 mW, photo-doping remains rather low, but it is the dominant contribution to the shift of the modes. Similar results were obtained on other samples including exfoliated 1L-MoS_2. The effects were found irreversible in some cases when P_λ exceeded 1 mW but remained always reversible if P_λ was kept below 1 mW.

Based on the above information, all Raman results reported and discussed in this paper were obtained by using a P_λ around

0.1 mW chosen as a good compromise between mitigating laser effects and maintaining measurement efficiency to ensure the accuracy of the Raman criteria discussed in the next part of this paper.

In summary, unless specified otherwise, all Raman spectra reported and discussed in this paper were recorded at an excitation wavelength of 532 nm, with a laser working-power close to 0.1 mW, and using a 100× objective (N.A. 0.9), on MoS_2 flakes or thin films deposited on SiO_2/Si substrate with a SiO_2 thickness of 90 ± 6 nm.

Application of Raman criteria to characterize MoS_2 flakes

In this part, we report and discuss the advantages and limits of some Raman criteria that were found to be efficient to derive the thickness (i.e., the number of layers N) of large MoS_2 flakes prepared by different ways, namely mechanical exfoliation and standard CVD (including twisted CVD 2L-MoS_2). Then, we discuss the application of Raman spectroscopy to characterize samples synthesized by DLI-PP-CVD. In contrast to the first two kinds of MoS_2 samples, the latter are constituted of nanoflakes with possibly a distribution of thicknesses and twist angles between adjacent layers of multilayer domains as well as a higher number of defects.

Exfoliated MoS_2 flakes as reference samples

We performed Raman experiments on mechanically exfoliated MoS_2 [1] that will serve as reference samples. The stacking sequence in exfoliated MoS_2 flakes is of the 2Hc-type [34]. The common feature of all these samples is to have a limited number of defects. Note also that all exfoliated flakes have a lateral size (few micrometers at minimum) significantly larger than the diameter of the laser spot. In such flakes, the exact number of layers, N, is determined by combining optical microscopy, spectral reflectivity, and the measurement of the breathing modes and shear modes in the ultralow frequency (ULF) range of the spectra [32-34].

One of the most popular criteria to determine the number of layers of MoS_2 flakes is the measurement of $\Delta\omega_{A-E}$, that is, the frequency difference between the A_{1g} and E^1_{2g} phonon modes [26,29,30]. Figure 3a shows the dependence of $\Delta\omega_{A-E}$ on the number of layers measured on exfoliated MoS_2 flakes deposited on Si/SiO_2 substrates with four different SiO_2 thicknesses. As previously well documented in the literature, we confirm that $\Delta\omega_{A-E}$ depends monotonously on the number of layers and does not depend on the SiO_2 thickness (Figure 3a). The separation between N and $N + 1$ values are larger than the experimental uncertainties (error bars in the graph) up to $N = 3$. The error bars start to overlap between $N = 4$ and $N = 5$. Comparison with data from the literature (see inset in Figure 3a) shows that this overlap occurs even between $N = 3$ and $N = 4$ when additional variability due to setup and samples is taken into account. Above $N = 4$, the separation becomes too small compared to the uncertainty. Thus, the measurement of $\Delta\omega_{A-E}$ in exfoliated MoS_2 flakes allows one to evaluate with good accuracy the number of layers for $N \leq 3$. It is then necessary to supplement the $\Delta\omega_{A-E}$ criterion with others to reliably count thick multilayers. In addition, we will establish in the following that this criterion has to be taken with care to derive N in MoS_2 samples other than reference exfoliated MoS_2, because the A_{1g} and E^1_{2g} frequencies, and thus the value of $\Delta\omega_{A-E}$, can be affected by different factors such as stacking order, strain, doping, and defects which can be present in MoS_2 flakes prepared by other ways [44,46-49].

To evaluate the number of layers, we can also use information associated with the integrated intensity of MoS_2 phonon modes. Figure 3b and Figure 3d show, respectively, the dependences of the normalized integrated intensities of the A_{1g} and the E^1_{2g} mode as functions of N for four values of the SiO_2 thickness. For normalization, we use here an external reference, which is a bare Si(111) wafer with only native oxide. In the following, $A(Si_{111})$ stands for the integrated intensity of the Si(111) 521 cm^{-1} mode. This reference is preferred to the Si(100) substrate with 90 ± 6 nm SiO_2 to avoid the effects of the SiO_2 thickness variations and crystal orientation. For comparison with other setups or references, the polarization ratio of our setup and the relative values measured on Si(100) with native oxide and 90 nm SiO_2 are given in Supporting Information File 1. As noted by several authors and predicted by the optical interference model, the normalized integrated intensities of MoS_2 modes, namely $A(A_{1g})/A(Si_{111})$ and $A(E^1_{2g})/A(Si_{111})$, increase first with N and then decrease showing a maximum for $N = 4$–5 for all SiO_2 thicknesses. Obviously, this non-monotonous dependence prevents using these measurands alone to evaluate the number of layers for $N > 4$. Moreover, a significant dependence of the MoS_2 Raman intensity on the SiO_2 thickness occurs for $N > 2$, pointing out the importance to determine precisely this latter parameter.

Another criterion to derive the thickness of MoS_2 flakes is the $A_{2D}(Si)/A_0(Si)$ intensity ratio [31]. For the evaluation of this ratio, it is of great practical advantage to use the same silicon (the silicon below the oxide, which is Si(100) in the present work) in the measurement of $A_{2D}(Si)$ and $A_0(Si)$. A necessary precaution is that the Si(100) substrate orientation has to be kept the same for both measurements. Another advantage is to give a common origin to the plots of $A_{2D}(Si)/A_0(Si)$ as a function of N ($A_{2D}(Si)/A_0(Si) = 1$ for $N = 0$) for any SiO_2 thickness.

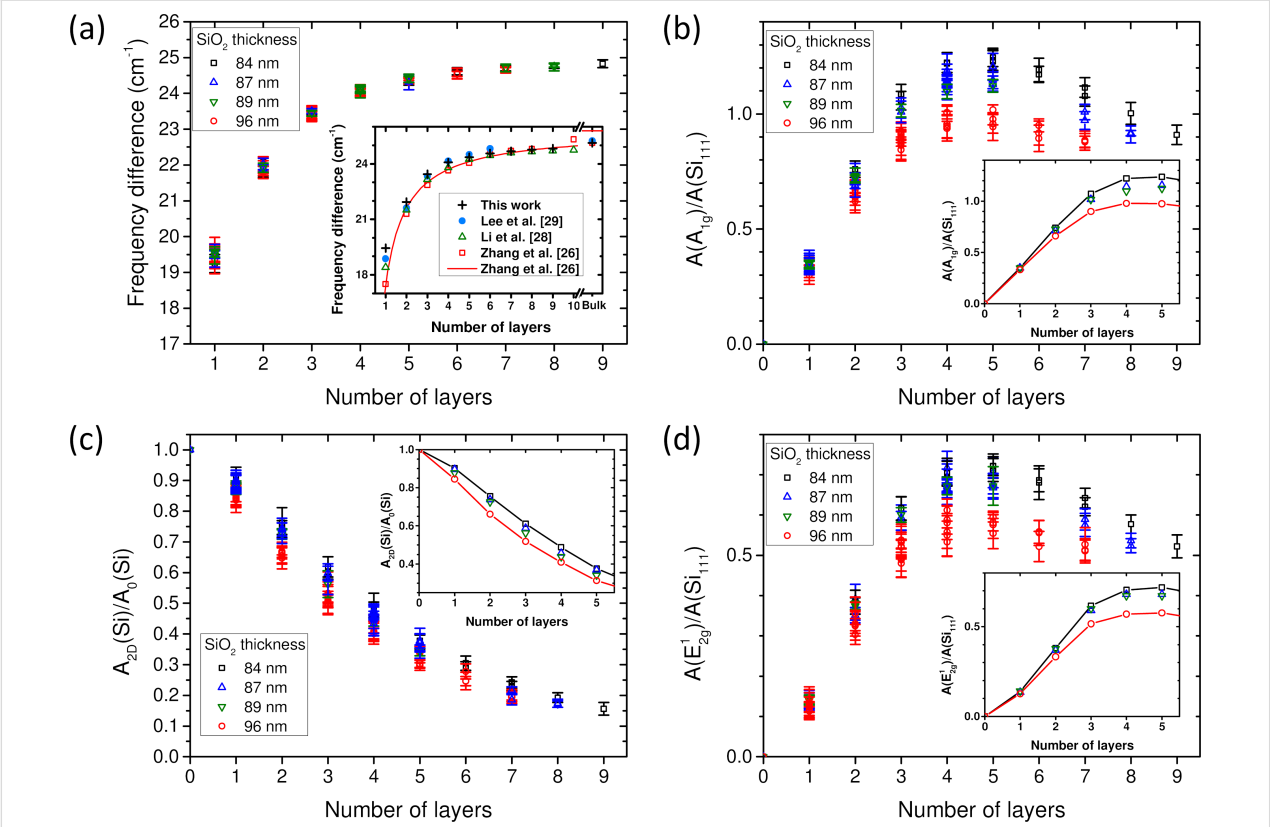

Figure 3: Mechanically exfoliated samples on SiO_2/Si substrates with four different SiO_2 thicknesses specified in the legends. Dependence on the number of MoS_2 layers (a) of the frequency difference between the A_{1g} and E^1_{2g} phonon modes, and of the normalized integrated intensities (see text) of (b) the A_{1g}, (c) the Si 521 cm^{-1}, and (d) the E^1_{2g} modes. The inset in (a) shows a comparison of the average values measured here with data from the literature. The insets in (b–d) show the corresponding average values for each SiO_2 thickness and each number of layers.

Figure 3c displays the $A_{2D}(Si)/A_0(Si)$ ratio measured on exfoliated MoS_2 flakes deposited on SiO_2/Si(100) substrates with four different SiO_2 thicknesses as a function of N. We confirm the monotonous decrease of the $A_{2D}(Si)/A_0(Si)$ ratio with increasing N [31]. For each N, the value of this ratio depends on the SiO_2 thickness (Figure 3c; black, blue, green, and red symbols correspond to a SiO_2 thickness of 84, 87, 89, and 96 nm, respectively). Despite the monotonous dependence of the $A_{2D}(Si)/A_0(Si)$ ratio, its dependence on SiO_2 thickness combined with experimental errors lead to the conclusion that the measured values for N and $N + 1$ can overlap for any N if the SiO_2 thickness is not known with good accuracy. For a given SiO_2 thickness, the gap between the $A_{2D}(Si)/A_0(Si)$ ratio for N and $N + 1$ is sufficient to ensure a rather good reliability only for $N \leq 5$.

In summary, for exfoliated MoS_2, considering jointly the three Raman criteria (i) value of $\Delta\omega_{A-E}$, (ii) value of the normalized integrated intensities of the A_{1g} and E^1_{2g} modes, and (iii) value of the $A_{2D}(Si)/A_0(Si)$ ratio, one can unambiguously derive the number of layers as long as $N \leq 4$ and the SiO_2 thickness is precisely known. It has also been suggested in the literature to use the intensity ratio $A(A_{1g})/A_{2D}(Si)$ (or equivalently $A(E^1_{2g})/A_{2D}(Si)$). As it will be discussed in the following, we see two major problems with this approach. The first is the dependence of the Si signal on the crystal orientation and the SiO_2 thickness. The second relates to the fact that using this ratio, rather than using each measurand independently and contrasting them, even if more practical, can hide some information.

Finally, we compare in Supporting Information File 1, Figure S3, the dependence on N of $A(A_{1g})/A(Si_{111})$ and $A_{2D}(Si)/A_0(Si)$ for three SiO_2 thicknesses and two microscope objectives with different numerical apertures, N.A. = 0.9 (blue symbols in Figure S3), and N.A. = 0.5 (red symbols in Figure S3). We observe that the normalized integrated intensity of the A_{1g} mode, $A(A_{1g})/A(Si_{111})$ (Figure S3a–c), is independent of the value of N.A. Concerning the dependence on N of $A_{2D}(Si)/A_0(Si)$ (Figure S3d–f), we found that this ratio is slightly smaller for N.A. = 0.5 than for N.A. = 0.9 and is in a better agreement with the model of Li and coworkers [31] (black solid line in Figure S3d–f). (Note that in this latter work the experimental data on which the model has

been adjusted were recorded using a numerical aperture N.A. ≈ 0.45).

MoS_2 flakes prepared by CVD

In this part, we analyze the pertinence of the previous criteria to derive the thickness of large MoS_2 flakes synthesized by CVD. In a first part, we probe the effectiveness of these criteria to evaluate the thickness of large standard CVD MoS_2 flakes. Such flakes have a limited number of defects and, like in exfoliated MoS_2, the stacking sequence is of the 2Hc type. In the second part, we examine the relevance of these criteria to evaluate the thickness of twisted CVD MoS_2 flakes.

Standard CVD MoS_2 flakes: As derived from the features of the LB and S ultralow-frequency modes, these samples do not show any twist between adjacent layers (presence of S modes for all flakes with $N \geq 2$). The flakes are thus characterized by 2Hc stacking (or close to 2Hc stacking) and a low number of defects, and are named standard CVD MoS_2 flakes. On the basis of the latter features, the structure of these flakes is close to that of exfoliated MoS_2 flakes. However, the high temperature used in the CVD synthesis and interaction with the substrate can lead to lattice distortion and the presence of vacancies and doping. In the following, we limit our study to a number of layers $N \leq 4$.

Figure 4a compares the values of $\Delta\omega_{A-E}$ measured on exfoliated (Figure 4a, black symbols) and standard CVD MoS_2 flakes (Figure 4a, red symbols) for $N \leq 4$. As previously, the exact number of layers is obtained by combining optical microscopy, spectral reflectivity, and number and frequencies of LB and S modes. For both kinds of MoS_2 flakes, $\Delta\omega_{A-E}$ increases monotonously with N, but for the same N, the values of $\Delta\omega_{A-E}$ are systematically larger in standard CVD MoS_2 flakes. We attribute this discrepancy mainly to a difference of strain states between the two kinds of samples. Exfoliated samples are mostly found with low or slight compressive strain, while CVD samples are under tension. Other factors such as doping, defects,

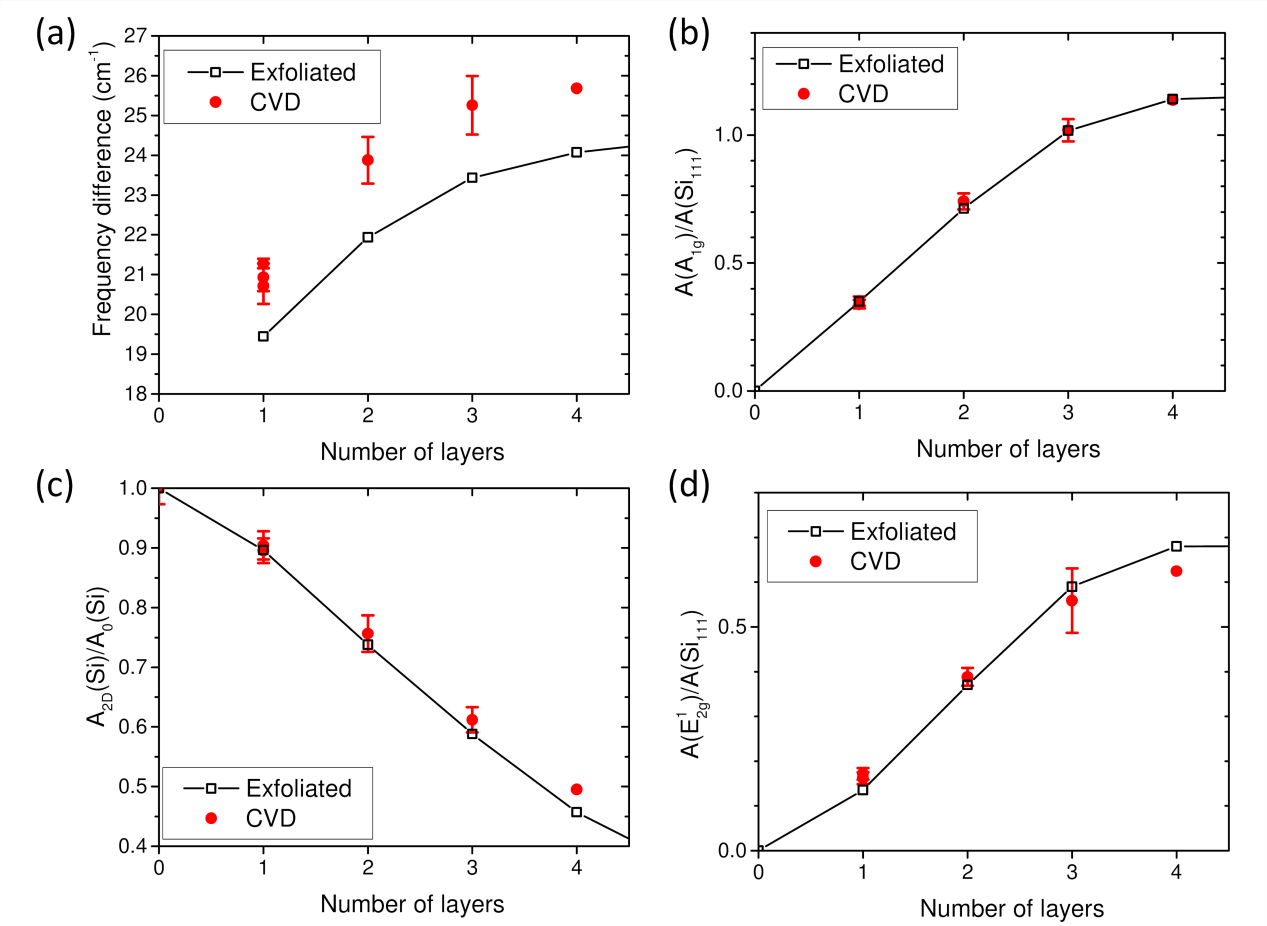

Figure 4: Comparison between CVD (red filled dots) and mechanically exfoliated (black-line-connected open squares) MoS_2 on a 87 nm SiO_2/Si substrate. Dependence on the number of MoS_2 layers of (a) the frequency difference between the A_{1g} and E^1_{2g} phonon modes, and of the normalized integrated intensities (see text) of (b) the A_{1g}, (c) the Si 521 cm^{-1}, and (d) the E^1_{2g} modes. For the 4L CVD, only few points are measured and the errors are not shown because they cannot be properly derived.

or stacking were shown to lead to large changes of $\Delta\omega_{A-E}$ [44,46,49]. In summary, the value of $\Delta\omega_{A-E}$ is clearly and significantly sample-dependent. Consequently, $\Delta\omega_{A-E}$ cannot be considered as a definitive criterion to derive the number of layers in any of MoS_2 flakes prepared in different ways. In other words, one cannot define a single master curve, $\Delta\omega_{A-E}$ vs N, which would be valid for all the MoS_2 flakes independently of their preparation method or environment.

The dependencies on N of the normalized integrated intensities of A_{1g} and E^1_{2g} modes and the $A_{2D}(Si)/A_0(Si)$ ratio measured on standard CVD flakes are compared with the average values of exfoliated samples with the same substrate SiO_2 thickness (Figure 4b–d). In contrast to $\Delta\omega_{A-E}$, the N dependencies of these intensities are very close in exfoliated and standard CVD MoS_2 flakes. Only $A_{2D}(Si)/A_0(Si)$ and the normalized integrated intensity of the E^1_{2g} phonon modes slightly differ for $N = 4$. However, this may be due to the fact that the statistics is rather poor on this measurement, because this flake is rather small compared to the others. With regards to these results, these measurands give important information to evaluate the number of layers of 2Hc-stacked MoS_2 flakes independently of the elaboration procedure as long as $N \leq 4$.

Twisted CVD MoS_2 flakes: Other interesting samples are large CVD MoS_2 flakes that present a twist angle, θ, between adjacent layers. We exemplify here the complexity to characterize such samples from the previous Raman criteria with the case of twisted MoS_2 bilayers. The identification of the bilayer character of the investigated flakes was unambiguously obtained independently from spectral reflectivity and optical contrast.

Figure 5a shows the low-frequency range of spectra recorded on three types of MoS_2 bilayer (named 2L-MoS_2 in the following),

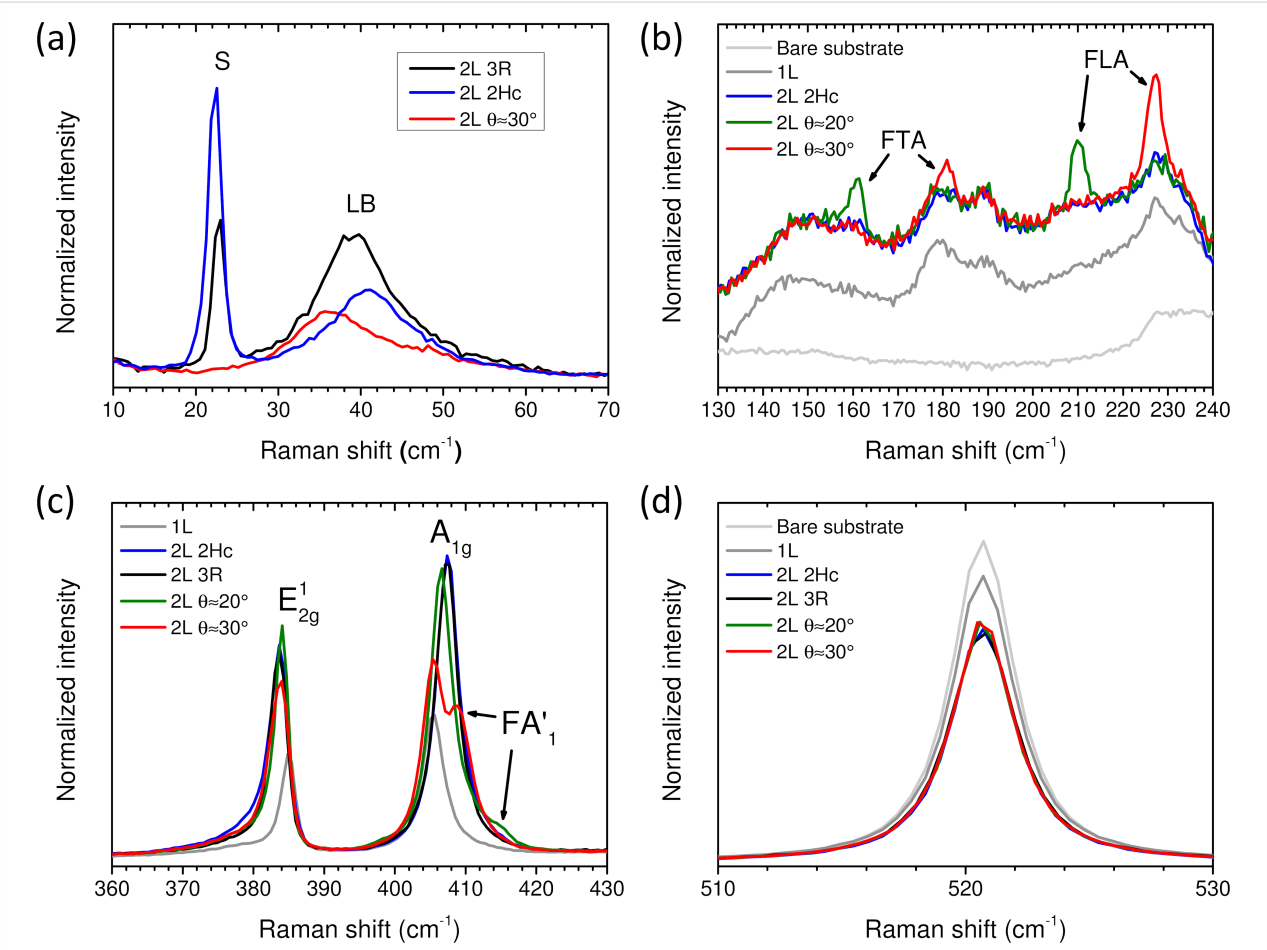

Figure 5: θ-2L-MoS_2. (a) Raman spectra of 3R-, 2Hc- and 30°-2L-MoS_2 (black, blue, and red lines, respectively) in the ultralow-frequency region. Layer breathing (LB) and shear (S) modes are labelled. (b) Raman spectra of 2Hc-, 20°- and 30°-2L-MoS_2, 1L-MoS_2, and bare substrate in the region of 130–240 cm^{-1}. Raman modes with θ-dependent frequencies (FTA and FLA) are labelled. (c) Raman spectra of 2Hc-, 3R-, 20°- and 30°-2L-MoS_2, and 1L-MoS_2 in the region of 360–430 cm^{-1}. E^1_{2g}, A_{1g}, and θ-dependent FA'_1 are labelled. (d) Raman spectra of 2Hc-, 3R-, 20°- and 30°-2L-MoS_2, 1L-MoS_2, and bare substrate in the region of the Si 521 cm^{-1} mode. Y-scale intensities are normalized to the incident laser power and the acquisition time. Presented spectra are averages extracted from Raman maps.

namely a bilayer with θ ≈ 30° (this sample belongs to the so-called twisted-bilayer family for which 0 < θ < 60° and is named in the following as θ-2L-MoS_2), the so-called 2Hc-2L-MoS_2 and the so-called 3R-2L-MoS_2. In the latter structure, the stacking between two adjacent layers corresponds to a twist angle of θ = 0°, and it is such that the S atoms of the top monolayer are superimposed on the Mo atoms of the bottom monolayer, and the Mo atoms of the top monolayer are above the hexagon centers of the bottom monolayer [50]. The spectrum in the low-frequency range is dominated by the contributions of the LB and S modes, the frequencies of these modes depending on the twist angle [20,39]. The LB mode emerges in the Raman spectra of all 2L-MoS_2 samples. In line with previous results [20], the Raman shift of the peak position of the LB mode in 3R-2L-MoS_2 is smaller than that of the 2Hc-2L-MoS_2, and the LB mode Raman shift in 30°-2L-MoS_2 is even smaller. Also, in agreement with the literature [20,38-41], the S mode vanishes in 30°-2L-MoS_2.

In Figure 5b, the 130–240 cm^{-1} range of the Raman spectra recorded on monolayer, 2Hc-2L-MoS_2, and two θ-2L-MoS_2 is displayed. As well documented in the literature, this frequency range is dominated by the contributions of second-order Raman processes [20,26]. The general profile of the spectra is similar in 1L-MoS_2, 2Hc-2L-MoS_2, and θ-2L-MoS_2 with the exception that in the latter flakes, new bands, named FLA and FTA, are superimposed to the second-order Raman spectra. The FLA and FTA modes in θ-2L-MoS_2 are attributed, respectively, to folded longitudinal acoustic phonons and folded transverse acoustic phonons of the monolayer due to the presence of a moiré superlattice [20]. As shown in the literature [20], the frequencies of these modes depend on the twist angle (see Figure 2e in [20]). Unfortunately, these dependencies show a mirror behavior with respect to θ = 30°. This means that from given FLA and FTA positions, two values are possible: θ ∈ [0,30]° or its mirror 60° − θ. As a consequence, θ will be given in the range of 0–30° in all plots in Figure 6 with the possibility that the values attributed to θ-2L-MoS_2 could be 60° − θ instead. For instance, the data from both 2Hc-2L-MoS_2 and 3R-2L-MoS_2 are reported at θ = 0° in these plots. From the positions of the FTA and FLA, we claim that the spectra of the two θ-2L-MoS_2 displayed in Figure 5 correspond to 20°-2L-MoS_2 (Figure 5b–d, solid green line) and 30°-2L-MoS_2 (Figure 5a–d, solid red line), respectively.

The dependence of A_{1g} and E^1_{2g} modes on the twist angle (derived from the positions of FTA and FLA modes) is reported in Figure 5c. The frequency of the E^1_{2g} mode in 3R-, 2Hc-, and θ-2L-MoS_2 is downshifted with respect to its frequency in 1L-MoS_2, and it does not show a clear dependence on the twist angle. In contrast, the profile of the A_{1g} mode significantly depends on the twist angle, and a new mode, named FA'_1, appears on the high-frequency side of the A_{1g} mode. The FA'_1 mode is identified as Raman scattering from moiré phonons associated with the A'_1 dispersion curve of 1L-MoS_2. It is folded onto the zone center and, consequently, becomes Raman active [20]. Obviously, its frequency depends on the twist angle and the θ-dependence of the FA'_1 frequency was recently established both theoretically and experimentally (see Figure 3e in [20]). On the basis of these previous results, we have been able to evaluate the value of θ for each 2L-MoS_2 investigated from the position of the FA'_1 mode. The values of the angles derived from the position of FTA/FLA and FA'_1 are in close agreement.

The objective of this work is to characterize the thickness of all MoS_2 flakes. The relevance of the criteria based on the frequency ($\Delta\omega_{A-E}$) and normalized integrated intensity ($A(A_{1g})/A(Si_{111})$) of the A_{1g} mode has to be reevaluated in twisted 2L-MoS_2 flakes. As shown in Figure 5d, the normalized intensity of the 521 cm^{-1} Si mode from the substrate underneath MoS_2 flakes is close in all the 2L-MoS_2 and independent of the twist angle.

Figure 6 summarizes and details the dependence on the twist angle of the four Raman criteria defined above for 2L-MoS_2. In all plots of Figure 6, the values of angles were derived from the positions of FTA, FLA and FA'_1. The values of the different criteria measured for θ-2L-MoS_2 are compared with the average values of the same criteria measured on exfoliated 1L-, 2L-, and 3L-MoS_2 flakes. In θ-2L-MoS_2, the value of $\Delta\omega_{A-E}$ strongly depends on the twist angle and significantly differs from the average value measured in 2Hc-2L-MoS_2 (Figure 6a). For θ = 30°, the value of $\Delta\omega_{A-E}$ is close to the one found in CVD 1L-MoS_2 [51]. In consequence, using $\Delta\omega_{A-E}$ alone could lead to a wrong evaluation of the thickness of twisted 2L-MoS_2.

The normalized integrated intensity $A(A_{1g})/A(Si_{111})$ significantly decreases when the twist angle increases (Figure 6b, red dots), and in 30°-2L-MoS_2, the value of $A(A_{1g})/A(Si_{111})$ is close to the average value found in 1L-MoS_2 (Figure 6b, blue solid line). The behavior of $A(A_{1g})/A(Si_{111})$ is opposite to the one of the normalized integrated intensity of the FA'_1 mode, $A(FA'_1)/A(Si_{111})$, the latter increasing with the twist angle (Figure 6b, gray squares). These results are in qualitative agreement with those reported in [40]. It can be emphasized that the integrated intensity of A_{1g} and FA'_1 bands taken together (Figure 6b, orange triangles) is close to the average value found for 2Hc-2L-MoS_2 (Figure 6b, red solid line). The reason for this compensation between $A(A_{1g})$ and $A(FA'_1)$ is not clear yet, but it could present a practical advantage in the use of the global integrated intensity of the spectral band, located around the po-

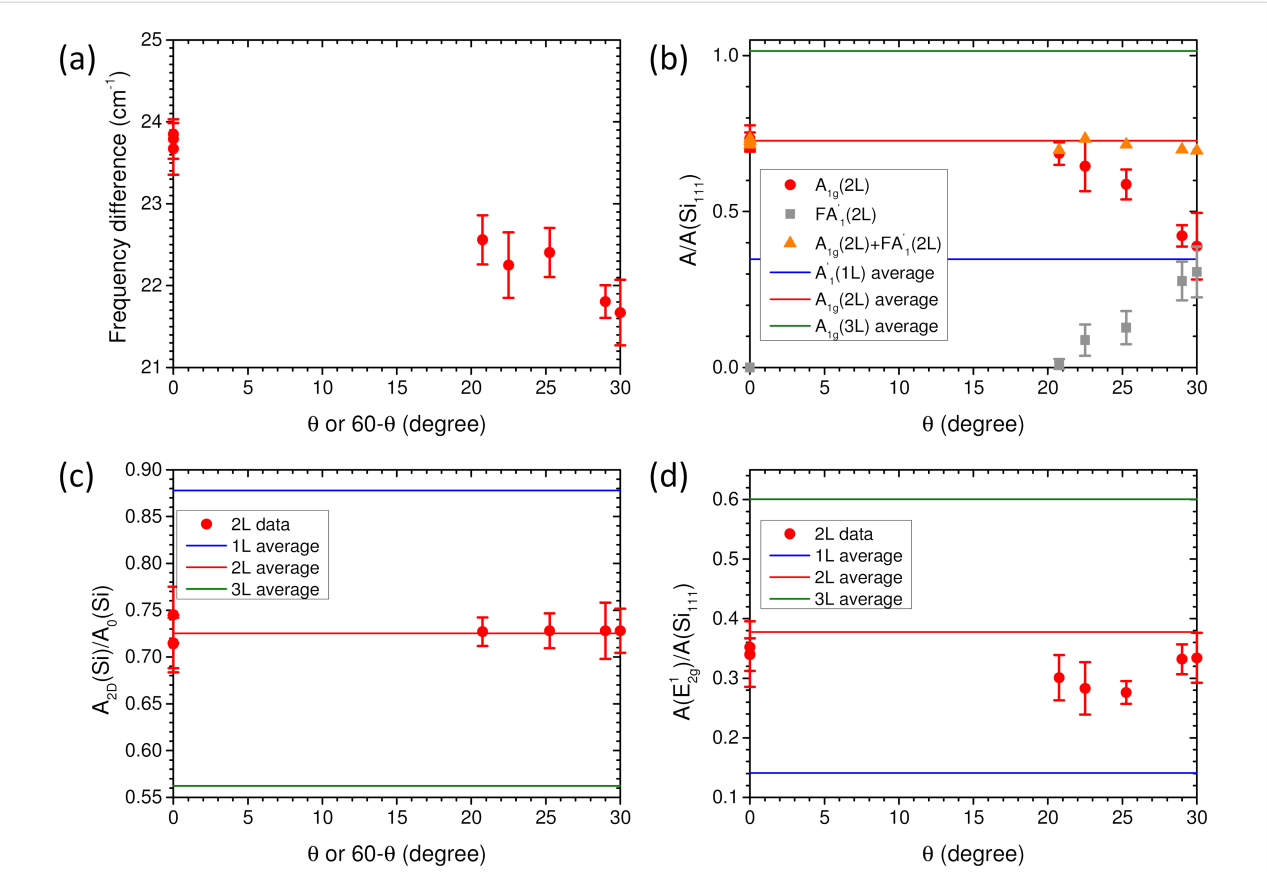

Figure 6: θ-2L-MoS_2. θ-dependence of the frequency difference between the A_{1g} and E^1_{2g} phonon modes (a); θ-dependence of the normalized integrated intensities (see text) of A_{1g} and FA'_1 modes and their sum (b), of the Si 521 cm^{-1} mode (c), and of the E^1_{2g} mode (d). In (b–d), the corresponding average values for 1L-MoS_2, 2Hc 2L-MoS_2, and 3L-MoS_2 are plotted as horizontal lines (blue, red, and green, respectively) for comparison.

sition of the A_{1g} mode for the evaluation of the thickness of twisted MoS_2 flakes.

We also observed a tendency for $A(E^1_{2g})/A(Si_{111})$ to be slightly lower for θ-2L-MoS_2 than for 2Hc-2L-MoS_2 (or 3R-2L-MoS_2, which is similar), but to a lesser extent compared to $A(A_{1g})/A(Si_{111})$, that is ca. 20% vs ca. 50% at maximum, respectively (Figure 6d). These results are also in qualitative agreement with those reported in [40]. Finally, only the value of the $A_{2D}(Si)/A_0(Si)$ ratio seems to provide a robust/reliable information to characterize the thickness of MoS_2 flakes, since it is found largely independent of θ in all measured 2L-MoS_2 samples (Figure 6c). Even if further work is needed to complete the data presented here with other values of θ and twisted MoS_2 samples with $N > 2$, we anticipate that the value of $A_{2D}(Si)/A_0(Si)$ ratio would be close in twisted and 2Hc-stacked MoS_2 multilayers. However, as previously recalled, the sensitivity of this ratio to the SiO_2 thickness and the gap between the $A_{2D}(Si)/A_0(Si)$ ratios for N and $N + 1$ permit to ensure the determination of N with a rather good reliability only for $N \leq 5$.

DLI-PP-CVD MoS_2 nanoflakes

The aim of this part is to define which Raman information is relevant to estimate the thickness of MoS_2 samples produced by DLI-PP-CVD. These samples are significantly different from the previous ones (exfoliated and standard CVD). Indeed, they are constituted of nanoflakes (with a lateral size of typically 50 nm, i.e., well below the laser spot size) with possibly a distribution of thicknesses and twist angles between adjacent layers of multilayer domains and a higher number of defects (the average inter-defect distance ranges from 3 to 6 nm as estimated from the LA and A_{1g} intensity ratio [52]). In addition, the MoS_2 surface coverage is a priori unknown and can be incomplete. It is then necessary to implement a first check criterion that ensures that the thickness estimation method based on the comparison with results obtained on exfoliated samples is still valid. More generally, this point is critical for the characterization of samples synthesized using new methods or new precursors that can lead to the co-deposition of several by-products (such as carbon, oxides, and metals), which can significantly change the measured Raman intensities. Based on the results presented in the previous sections, we have shown that the value of the

$A_{2D}(Si)/A_0(Si)$ ratio provides a robust/reliable Raman information to characterize the thickness of MoS_2 flakes for $N \leq 5$. However, this parameter does not rely unambiguously on the presence of MoS_2. The deposition of any other material would influence its value and could lead to a wrong estimation. In the most general case, the sample characteristics are not perfectly known and can be significantly different from the reference characteristics. As a consequence, it seems mandatory to compare the thickness estimated from the $A_{2D}(Si)/A_0(Si)$ ratio with other measurands directly related to the presence of MoS_2. To this aim, we propose to use jointly the normalized integrated intensity of the MoS_2 phonon modes, namely $A(A_{1g})/A(Si_{111})$ and/or $A(E^1{}_{2g})/A(Si_{111})$.

In Figure 7, the values of $A(A_{1g})/A(Si_{111})$ (Figure 7a) and $A(E^1{}_{2g})/A(Si_{111})$ (Figure 7b) are plotted as functions of the value of $A_{2D}(Si)/A_0(Si)$. In these graphs, the data obtained on DLI-PP-CVD samples are compared with the average reference measurements established previously on exfoliated MoS_2 deposited on Si/SiO_2 substrate with the same SiO_2 thicknesses, namely 96 nm (red open dots in Figure 7) and 87 nm (blue open dots in Figure 7). Note that in the exfoliated samples, the exact number of layers N is perfectly known and given on the plots of Figure 7 close to corresponding open dots. The idea behind this representation comes from the expectation that the presence of contaminations or deposition of others species would have a different impact on the Raman intensity coming from MoS_2 in the film and on the one coming from the Si substrate underneath the deposited thin film. It is, thus, expected that the measurements on contaminated or highly defective MoS_2 thin films will fall off the reference curve. Indeed, data obtained on poorly crystalline MoS_2 films synthesized by DLI atomic layer deposition (not shown) are found systematically and significantly below the corresponding reference curve. Concerning the DLI-PP-CVD samples presented in Figure 7, the $A(A_{1g})/A(Si_{111})$ vs $A_{2D}(Si)/A_0(Si)$ dependence is found fully compatible with the respective reference exfoliated curves (Figure 7a). The $A(E^1{}_{2g})/A(Si_{111})$ vs $A_{2D}(Si)/A_0(Si)$ data points mainly agree for thin layers ($A_{2D}(Si)/A_0(Si) > 0.8$) but fall systematically below the corresponding reference exfoliated curves for thicker layers ($0.8 > A_{2D}(Si)/A_0(Si) > 0.6$) as shown in Figure 7b.

Another way to compare the results is estimating the thickness of DLI-PP-CVD samples by interpolation from exfoliated data of the measured values for $A_{2D}(Si)/A_0(Si)$, $A(A_{1g})/A(Si_{111})$, and $A(E^1{}_{2g})/A(Si_{111})$. In Figure 8a (respectively 8b), the average number of layers ($\bar{N}$) obtained using $A(A_{1g})/A(Si_{111})$ (respectively $A(E^1{}_{2g})/A(Si_{111})$) are plotted as a function of the number derived from $A_{2D}(Si)/A_0(Si)$. It can be emphasized that non-integer values are found for $\bar{N}$, indicating the presence of a mix with unknown proportions of bare substrate (0L), 1L-MoS_2, 2L-MoS_2, 3L-MoS_2, and so on in the investigated DLI-PP-CVD films. It is also noticeable that the errors of $\bar{N}$ estimated from $A(A_{1g})/A(Si_{111})$ become larger when $\bar{N}$ is close to 3 as a consequence of the smoother dependence of this parameter with $\bar{N}$. In agreement with the conclusion drawn above from Figure 7, Figure 8a illustrates the coherence between the values of $\bar{N}$ derived from $A(A_{1g})/A(Si_{111})$ and $A_{2D}(Si)/A_0(Si)$. All data remain close to the red solid line that represents the ideal relation $y[\bar{N}$ via $A(A_{1g})/A(Si_{111})] = x[\bar{N}$ via $A_{2D}(Si)/A_0(Si)]$. Figure 8b as well confirms that the values of $\bar{N}$ derived from $A(E^1{}_{2g})/A(Si_{111})$ and $A_{2D}(Si)/A_0(Si)$ agree well for $\bar{N} < 1.5$, but

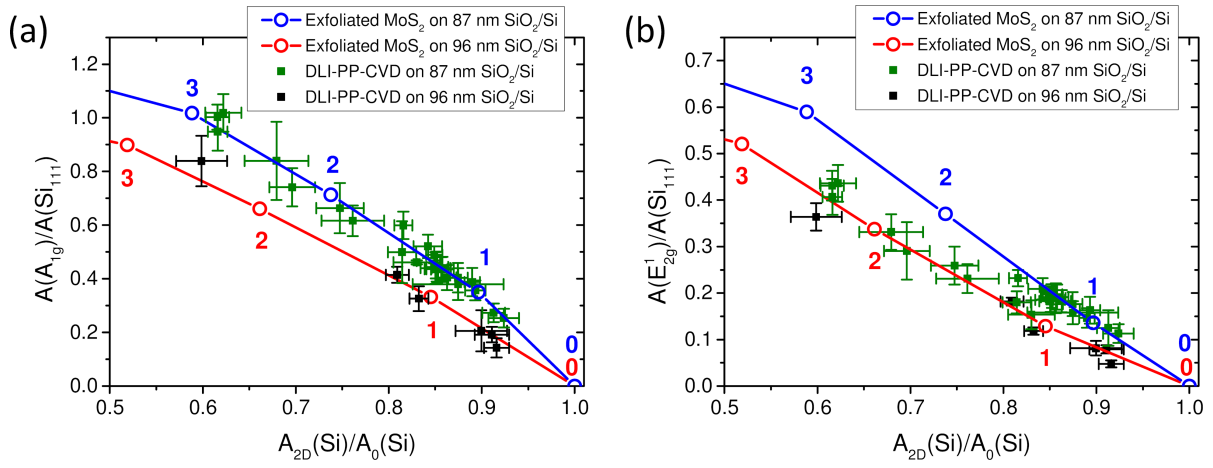

Figure 7: DLI-PP-CVD samples. Normalized integrated intensities of (a) the A_{1g} and (b) the $E^1{}_{2g}$ modes as functions of the normalized integrated intensities of the Si 521 cm^{-1} mode of DLI-PP-CVD samples on 87 nm (green squares) and 96 nm (black squares) SiO_2 on Si substrates. Each point corresponds to the average value extracted from 121-point Raman maps. The average values measured on corresponding exfoliated MoS_2 samples are also plotted for comparison as open dots (blue and red, respectively, for 87 nm and 96 nm SiO_2), and the corresponding number of layers are provided. The lines are guides to the eye.

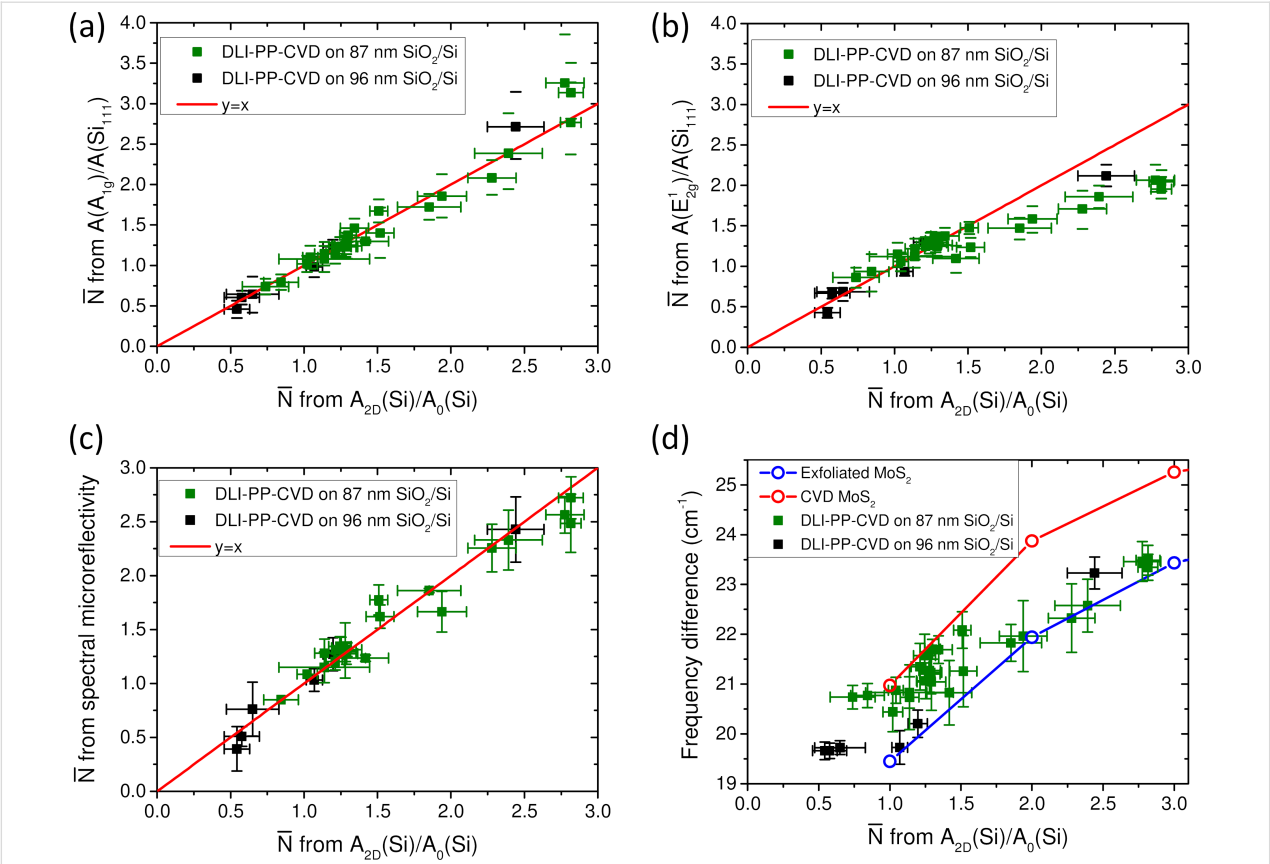

Figure 8: DLI-PP-CVD samples. Average number of layers of DLI-PP-CVD samples obtained by interpolation from exfoliated data of normalized integrated intensities of (a) the A_{1g} and (b) the E^1_{2g} modes, and of (c) microreflectivity spectra as functions of the average number of layers obtained by interpolation from exfoliated data of normalized integrated intensities of the Si 521 cm^{-1} mode. The red lines in (a–c) correspond to $y = x$. (d) Frequency difference between the A_{1g} and E^1_{2g} phonon modes of DLI-PP-CVD samples as a function of the average number of layers obtained by interpolation from exfoliated data of normalized integrated intensities of the Si 521 cm^{-1} mode. Green (respectively black) squares correspond to DLI-PP-CVD samples synthesized on 87 nm (respectively 96 nm) SiO_2/Si substrates. In (d), the average values measured on corresponding exfoliated (respectively CVD) MoS_2 samples are also plotted for comparison as open blue (respectively red) dots. The lines are guides to the eye.

the values of $\bar{N}$ from $A(E^1_{2g})/A(Si_{111})$ are systematically lower than those obtained from $A_{2D}(Si)/A_0(Si)$ when $\bar{N} > 1.5$. One explanation could the presence of a larger proportion of multilayer regions in the thicker samples, for which, if they are twisted, $A(E^1_{2g})/A(Si_{111})$ has been shown to be attenuated in the previous section. If so, the question then arises why the same behavior is not observed for $A(A_{1g})/A(Si_{111})$ contrary to what would be expected. A possibility could be that because of the observed broadening of the A_{1g} mode in DLI-PP-CVD samples (presumably due to local heterogeneities in terms of doping, strain, defects, or thickness), the FA'_1 mode becomes indistinguishable from the A_{1g} mode. As a consequence, the intensity of FA'_1 would merge with $A(A_{1g})$ and compensate its attenuation. Other explanations relying on the presence of defects or strain cannot be disregarded, and further works are needed to fully clarify this point.

In order to further confirm the validity of the estimations of $\bar{N}$ for DLI-PP-CVD samples, we compare in Figure 8c the $\bar{N}$ values derived from $A_{2D}(Si)/A_0(Si)$ with the ones obtained independently from spectral microreflectivity. A very good agreement is found between the two series of data, establishing definitively the relevance of the $A_{2D}(Si)/A_0(Si)$ ratio to give with good accuracy the average thickness of DLI-PP-CVD MoS_2 samples for $\bar{N} \leq 3$. This agreement justifies the use of the values of $\bar{N}$ derived from $A_{2D}(Si)/A_0(Si)$ as abscissa axis in the previous plots.

Finally, in Figure 8d the frequency difference between the A_{1g} and E^1_{2g} phonons is plotted as a function of $\bar{N}$ estimated from $A_{2D}(Si)/A_0(Si)$ for DLI-PP-CVD samples and compared to the data obtained on exfoliated and CVD MoS_2. DLI-PP-CVD data are distributed between the two curves obtained from the reference samples. This further confirms that this measurand cannot be used to evaluate with good accuracy their average thicknesses. Nevertheless this comparison can be informative, showing that samples with $\bar{N} < 1$ are most certainly mainly composed of 1L-MoS_2 and suggesting that the proportions of

2L-MoS_2, 3L-MoS_2, or more gradually increase with $\bar{N}$, which is compatible with AFM observations (not shown).

To get further insight on the number of layer distributions in DLI-PP-CVD samples, we have measured their ULF modes. Representative ULF spectra are shown in Figure 9a for samples with average thicknesses ranging from 0.6 up to 2.8 MoS_2 layers as estimated from $A_{2D}(Si)/A_0(Si)$. Up to $\bar{N}$ = 1.3, only the LB mode of 2L-MoS_2 is observed around 40 cm^{-1} [20,38-41], showing that these samples can only be composed of 1L-MoS_2 and twisted 2L-MoS_2 plus possibly uncovered (bare substrate) regions. For thicker samples, the S mode of 2L-MoS_2 around 24 cm^{-1} is additionally visible, as well as a signal between 25 and 30 cm^{-1}, corresponding to the LB and S modes of 3L-MoS_2 [32,33]. For $\bar{N} \geq 2.4$, the LB mode of 4L-MoS_2 is also present around 21 cm^{-1}; there may also be a weak signal around 17 cm^{-1} (corresponding to the LB mode of 5L-MoS_2) reflecting the presence of 5L-MoS_2. The S mode of 4L-MoS_2 could be present as well around 28 cm^{-1}, but it is hardly distinguishable from the LB and S modes of 3L-MoS_2. Thus, ULF Raman spectra give valuable qualitative information on the different N present in each sample. Quantitative information relies on the determination of the surface coverages for each N (σ_N), that is, the ratio between the surface covered by exactly N layers and the total surface. With N = 0 standing for the bare substrate and N_{max} being the largest number of layers present in the sample, the definition of the average number of layers $\bar{N}$ can be written as

$$\bar{N} = \sum_{N=1}^{N_{max}} \sigma_N \times N \qquad (1)$$

and the total coverage (including bare substrate areas) is obviously 100%:

$$\sum_{N=0}^{N_{max}} \sigma_N = 1 \qquad (2)$$

AFM imaging (see Supporting Information File 1, Figure S4) reveals that for $\bar{N}$ > 1.25, the surface is fully covered by MoS_2, that is, σ_0 = 0, which removes an unknown. In addition, for $\bar{N}$ < 1.3, there is no signature of more than two layers, and we can set $\sigma_{N\geq 3}$ = 0 with confidence. Hence, for 1.25 < $\bar{N}$ < 1.3, the set of Equations 1 and 2 simplifies to

$$\bar{N} = \sigma_1 \times 1 + \sigma_2 \times 2$$
$$\sigma_1 + \sigma_2 = 1$$

This allows one to readily determine the two remaining unknowns σ_1 and σ_2, since $\bar{N}$ is known from $A_{2D}(Si)/A_0(Si)$.

Hereafter, a linear relationship between the Raman signal I_{LB}^{2L}, which is the LB mode peak intensity of 2L (N = 2) areas (the broad but well-identified 40 cm^{-1} peak), and the surface coverage is assumed, namely $\sigma_2 = \alpha_2 I_{LB}^{2L}$. The ratio $\alpha_2 = \sigma_2 / I_{LB}^{2L}$ is determined from five samples (1.25 < $\bar{N}$ < 1.3) for which we now have both the coverage σ_2 and the Raman signal I_{LB}^{2L}.

Because α_2 is now known and assuming that the linearity between σ_2 and the Raman signal I_{LB}^{2L} holds (which should be a good approximation for the thin multilayers considered here), $\sigma_2 = \alpha_2 I_{LB}^{2L}$ can be obtained directly for all samples from the Raman spectra, and is thus no longer an unknown.

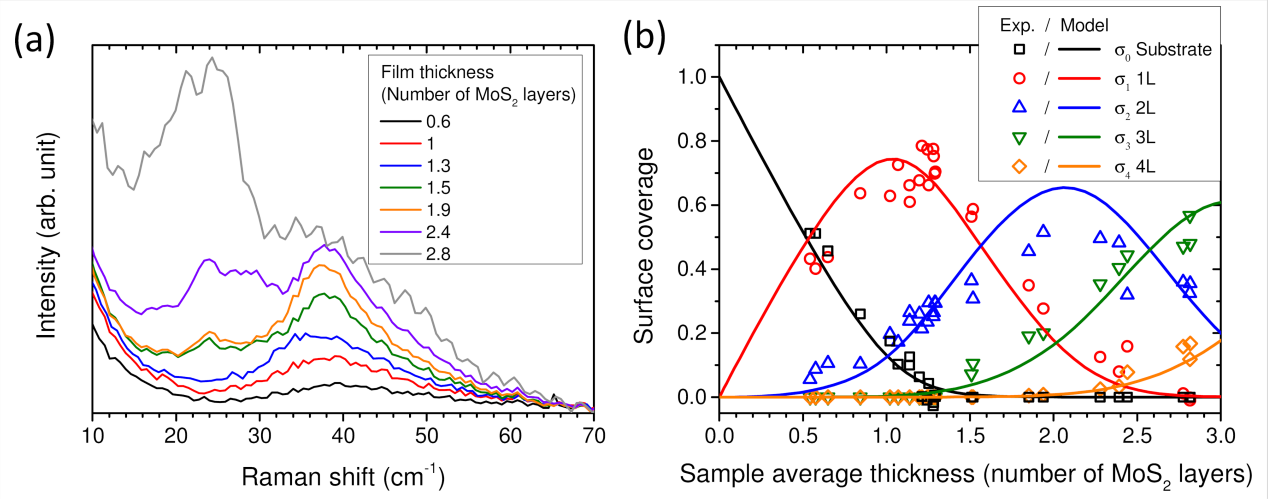

Figure 9: (a) Raman spectra in the ultralow-frequency region of selected DLI-PP-CVD samples with different average thicknesses as labelled in the legend. Presented spectra are averages extracted from 121-point Raman maps. (b) Surface coverages of bare substrate (black open squares), 1L-MoS_2 (red open dots), 2L-MoS_2 (blue open up-triangles), 3L-MoS_2 (green open down-triangles), and 4L-MoS_2 (orange open diamonds) as functions of the average DLI-PP-CVD sample thickness. The model results are shown as full lines. See the main text and Supporting Information File 1 for the description of the model.

We now turn to the samples with $\bar{N} < 1.25$, which may present some bare substrate areas, so σ_0 and σ_1 are a priori unknown. Both $\bar{N}$ and σ_2 are determined as explained above, and $\sigma_{N\geq 3} = 0$ is again a safe estimate. Hence, Equations 1 and 2 reduce to the system

$$\bar{N} = \sigma_1 \times 1 + \sigma_2 \times 2$$
$$\sigma_0 + \sigma_1 + \sigma_2 = 1$$

which may be solved trivially for σ_0 and σ_1.

A similar approach can be used for samples with $1.3 < \bar{N} < 2$ that are fully covered ($\sigma_0 = 0$) and might present some trilayers but show no trace of thicker layers. We set $\sigma_{N\geq 4} = 0$, and the system of equations reduces to

$$\bar{N} = \sigma_1 \times 1 + \sigma_2 \times 2 + \sigma_3 \times 3$$
$$\sigma_1 + \sigma_2 + \sigma_3 = 1$$

Both $\bar{N}$ and σ_2 are determined as explained above. Thus, the system can be trivially solved for the two remaining unknowns σ_1 and σ_3.

At this point it would be natural to get the proportionality between σ_3 and a Raman signal attributed to 3L areas ($N = 3$), and proceed recursively to obtain σ_4 in slightly thicker layers, and so on and so forth. In practice this becomes challenging because of the uncertainty on the 3L ($N = 3$) Raman signal, which is less clear than the 2L ($N = 2$) peak. Another approach gave better results.

Three samples with $\bar{N}$ between 2.75 and 2.85 are thick enough to neglect σ_0 and σ_1, yet thin enough for σ_5 to also be negligible as a first approximation. Equations 1 and 2 then reduce to

$$\bar{N} = \sigma_2 \times 2 + \sigma_3 \times 3 + \sigma_4 \times 4$$
$$\sigma_2 + \sigma_3 + \sigma_4 = 1$$

where $\bar{N}$ and σ_2 are known, so σ_3 and σ_4 can be determined readily.

The LB mode of 4L-MoS_2, located around 21 cm^{-1}, is sufficiently separated from other modes to be identified (which was not the case for I_{LB}^{3L}), so that I_{LB}^{4L} can be extracted from the spectra. From the three $2.75 < \bar{N} < 2.85$ samples $\alpha_4 = \sigma_4 / I_{LB}^{4L}$ is determined. Then, assuming again a linear relationship $\sigma_4 = \alpha_4 I_{LB}^{4L}$, the coverage by 4L ($N = 4$) layers can be determined for all samples. This removes another unknown.

Now the last remaining case of $2 < \bar{N} < 2.75$ samples can be solved, as

$$\bar{N} = \sigma_1 \times 1 + \sigma_2 \times 2 + \sigma_3 \times 3 + \sigma_4 \times 4$$
$$\sigma_1 + \sigma_2 + \sigma_3 + \sigma_4 = 1$$

give σ_1 and σ_3 directly, since $\bar{N}$, σ_2 and σ_4 are known.

The results obtained using this procedure are shown in Figure 9b where σ_N (with N from 0 to 4) is plotted as a function of $\bar{N}$, the average sample thickness. On this graph, all values of σ_2 (respectively σ_4) are calculated using I_{LB}^{2L} (respectively I_{LB}^{4L}) even for the samples used to derive the proportionality coefficient α_2 (respectively α_4). As shown in Figure 9b for samples with $1.25 < \bar{N} < 1.3$ (respectively $2.75 < \bar{N} < 2.85$), we find by this way $-0.03 < \sigma_0 < 0.04$ (respectively $-0.01 < \sigma_1 < 0.01$) with little fluctuations around the expected value of 0.

Just below the full coverage of the sample surface by MoS_2 ($\sigma_0 > 0$), both σ_1 and σ_2 increase with a slight tendency of σ_2 to increase faster than σ_1. Indeed, 1L-MoS_2 represents 80–90% of the deposited MoS_2 for $\bar{N} = 0.5$ and 70–80% for $\bar{N} = 1.3$. The maximum of σ_1 is reached around $\bar{N} = 1.3$ when the sample surface is totally covered by MoS_2 ($\sigma_0 = 0$), and σ_1 starts to decrease above this value. Around $\bar{N} = 1.6$, 1L-MoS_2 only represents 50% of the MoS_2. σ_2 continues to increase and reaches a maximum value of ≈50% around $\bar{N} = 2$ and then decreases for thicker samples. 3L-MoS_2 starts to appear after the substrate surface is completely covered by MoS_2 and increases continuously, representing about 50% of the thickest samples ($\bar{N} \approx 2.8$).

In order to verify our approach, we implemented a 2D growth toy model (see Supporting Information File 1 for details). The model results are shown in Figure 9b as full lines and give a good agreement with the experimental results. It should be noted that within this representation ($\sigma_N = f(\bar{N})$), the results of the model are remarkably robust to any parameter changes (the curves are almost insensitive to either doubling or halving the cell size and, thus, the advance rate, or to multiplying or dividing the growth rate by 5). In other words, this means that this comparison with the experiment cannot be used to validate any model parameters but demonstrates the relevance of the proposed procedure to estimate the σ_N from the experiments. Nevertheless, it has to be noted that while for $\bar{N} < 1.3$ the ULF Raman signature of 2L-MoS_2 remains very similar, it is not the case for thicker samples with the notable appearance of the S mode of 2L-MoS_2 around 24 cm^{-1} [32,33]. This could mean that the stacking order distribution changes. As a consequence, the hypothesis based on the proportionality between I_{LB}^{2L} and σ_2 would probably be less valid above $\bar{N} = 1.3$, and an error on the absolute values deduced can be expected. However, the appearance of the S mode of 2L-MoS_2 around 24 cm^{-1} could also be related to NL-MoS_2 (with $N \geq 3$) constituted of a stacking se-

quence where 2L are not twisted, for example, the so-called t(1+2)L, t(2+2)L, … structures [26,53]. In this case, our hypothesis would remain more appropriate. Despite this unknown as well as the other approximations made, we believe that the main tendencies can still be captured by the proposed analysis. Further works are needed to determine and improve the accuracy of the method.

Conclusion

In this work we have reviewed all Raman information leading to the evaluation of the thickness of MoS_2 flakes, that is, the layer number N. First, we have analyzed in detail the effects of some experimental parameters, namely the wavelength of the incident laser light used in the experiments, the power of the incident light, and the oxide thickness of the SiO_2/Si substrate on which the flakes are deposited, on the quality and accuracy of Raman results. Based on this analysis, an experimental protocol has been defined and systematically applied to large MoS_2 flakes (i.e., single-domain flakes much larger than the laser spot), including twisted MoS_2 flakes, prepared by different methods on the one hand and to MoS_2 thin films composed of nanoflakes prepared by the DLI-PP-CVD method on the other hand. Special attention was paid to the measurement statistics.

The limits of different Raman criteria which allow one to determine the thicknesses of MoS_2 flakes, namely (i) the value of $\Delta\omega_{A-E}$, (ii) the value of the normalized integrated intensity of A_{1g} and $E^1{}_{2g}$ MoS_2 modes, and (iii) the value of the $A_{2D}(Si)/A_0(Si)$ ratio, have been precisely studied in the different types of MoS_2 samples. We definitely confirm that $\Delta\omega_{A-E}$ cannot be considered a robust criterion to derive the number of layers in MoS_2 samples. We found that the value of the $A_{2D}(Si)/A_0(Si)$ ratio provides the most robust/reliable information to characterize the thickness of MoS_2 large flakes, especially since it is found largely independent of the twist angle. The limit of application of this criterion is $N \leq 5$, under the condition that the SiO_2 thickness is precisely known.

We then apply this analysis procedure to DLI-PP-CVD samples constituted of nanoflakes with a lateral size of typically 50 nm (well below the laser spot size) with possibly a distribution of thicknesses and twist angles between adjacent layers of multilayer domains and a higher number of defects. Our results definitively establish the relevance of the $A_{2D}(Si)/A_0(Si)$ ratio to give with good accuracy their average thickness $\overline{N}$, for $\overline{N} \leq 3$. Nevertheless, we emphasize that this criterion is not only related to the presence of MoS_2 and can be influenced by several factors, such as the co-deposition of by-products or the presence of defects, leading to a wrong estimation of $\overline{N}$. We propose to combine $A_{2D}(Si)/A_0(Si)$ with the normalized integrated intensity of the MoS_2 phonon modes, namely $A(A_{1g})$ and/or $A(E^1{}_{2g})$. Although limiting the application to $\overline{N} \leq 3$, this approach enables the validation of the $A_{2D}(Si)/A_0(Si)$ ratio to determine $\overline{N}$ in the presented case, and we anticipate that it would avoid possible errors in unfavorable situations.

Finally, to get further insight on the number of layer distributions in DLI-PP-CVD samples, we have measured their ULF modes. An original procedure based of the measurement of the intensity of the layer breathing modes allows one to evaluate the surface coverage (σ_N) for each N. A 2D growth toy model gives a good agreement with the experimental results supporting the proposed procedure to estimate the σ_N from the ULF spectra.

Experimental

Samples preparation

Mechanical exfoliation

MoS_2 flakes were obtained by micromechanical cleavage of a MoS_2 crystal (HQ graphene) using scotch tape (Nitto) and PDMS slabs (Gel-pak). They were then transferred onto Si substrates with SiO_2 layers of different thicknesses, namely 84, 87, 90, and 96 nm. Flakes were selected by optical microscopy and their thicknesses were determined by optical contrast.

Standard CVD process

MoS_2 was grown by CVD on 87 nm SiO_2 on Si substrates using MoO_3 (Sigma-Aldrich, 25 mg) and sulfur (Sigma-Aldrich, 250 mg) powders as solid precursors using a 1 inch quartz tube furnace. MoO_3 powder was placed in the center of the heating zone of the furnace, while sulfur was placed upstream at the furnace inlet. Prior to growth, air was evacuated by flowing Ar (ultrahigh purity, Linde) for 15 min at 200 sccm, after which the tube was heated to 200 °C for 10 min. The temperature was then increased to 750 °C under Ar (100 sccm), and it was held at this value for 15 min before cooling naturally to room temperature.

Direct-liquid injection pulsed-pressure chemical vapor deposition (DLI-PP-CVD)

The 12 × 11 mm SiO_2/Si (with 87 nm or 96 nm SiO_2 thicknesses) substrates were cleaned in acetone (C_3H_6O, technical, Acros Organics), isopropanol (C_3H_7OH, 99.8%, Höfer Chemie GmbH) and deionized water (H_2O, Acros Organics) under ultrasonic agitation for 10 min each, before being blown dry with nitrogen. They were then immediately loaded on the susceptor of the reaction chamber (Annealsys MC-050) for deposition. Solutions of 0.001 M molybdenum hexacarbonyl ($Mo(CO)_6$, 98%, Strem Chemicals) and 0.002 M sulfur (S, 99.999%, Acros Organics) in anhydrous toluene ($C_6H_5CH_3$, 99.8%, Sigma-Aldrich) were used as precursors. The process is

as follows: Following sample installation, the chamber is closed and brought to about 0.02 mbar. For monolayer depositions, it is imperative that the substrate is thoroughly cleaned and free of adsorbates. Therefore, to ensure complete desorption of remaining contaminants, the samples were kept for 30 min under vacuum at room temperature inside the deposition chamber. For the first part of the process, the pumping direction is reversed so that all species are pumped from the deposition chamber to the back of the reactor.

Nitrogen (800 sccm) is flowed through the chamber (200 sccm through the gas line, and 600 sccm through two injection heads) and the substrates are brought to 750 °C at a ramp of 2 °C/s. The reactor is kept in this state for 5 min for homogenization purposes. While still in reverse direction pumping, 0.3 g/min of both precursors are injected and vaporized to prepare the evaporation system for deposition. Then, the $Mo(CO)_6$ injection is stopped, the pumping direction is switched back to the deposition direction and hydrogen (40 sccm) is added to the gas mix. For 1 min, sulfur is injected to clean any remaining contaminants, and to prepare the surface of the substrate for MoS_2 deposition, then the deposition works in 20 s cycles. During one cycle, a single pulse of 3 to 10 ms of $Mo(CO)_6$ is injected while the S injection is set to 0.3 g/min. This 20 s cycle is repeated 80 to 160 times. The quantity of MoS_2 deposited is controlled by the quantity of $Mo(CO)_6$ injected, that is, the pulse duration and the number of cycles.

Raman spectroscopy

Raman spectra and maps were recorded using an Acton spectrometer fitted with a Pylon CCD detector and a 1800 grooves/mm grating (≈0.6 cm^{-1} between each CCD pixel). The samples were excited with a 532 nm (2.33 eV) laser (Newport Millennia Prime or Cobolt Samba) throughan Olympus microscope objective either 100× (numerical aperture 0.9) or 50× (numerical aperture 0.5). The full width at half-maximum (FWHM) of the focused laser spot with the 100× objective is about 380 nm. Optimized focus conditions were checked for each measurement. The samples were mounted on a three-axis piezoelectric stage (Physik Instrumente) to ensure the precise positioning and focusing of the laser spot. A Si(111) wafer with only native oxide sample was used as a daily reference for the system. The laser power was continuously measured during acquisitions allowing for intensity normalizations of the Raman spectra at each point of the maps. All data presented in this paper, unless specified otherwise, are extracted from Raman maps constituted by hundreds to thousands points (see Supporting Information File 1 for an example), which were analyzed using a custom-made software. All reported points are the average values obtained by Gaussian fitting of the data distribution extracted from Raman maps (corresponding to hundreds to several thousands of spectra), and the error bars correspond to 99.7% confidence intervals (±3 standard deviations).

2D growth toy model

The model used the DynamicGrids.jl package, which was part of the Dispersal.jl framework [54], see Supporting Information File 1 for more details.

Supporting Information

Supporting Information File 1 contains additional figures with an example of Raman maps, the Si mode as a function of the laser power, a comparison between two microscope objectives, other intensity references, atomic force microscopy images, and details of the 2D growth toy model. Supporting Information File 2 is a recording of the growth simulation.

Supporting Information File 1

Additional experimental data.
[https://www.beilstein-journals.org/bjnano/content/supplementary/2190-4286-15-26-S1.pdf]

Supporting Information File 2

Recording of the growth simulation.
[https://www.beilstein-journals.org/bjnano/content/supplementary/2190-4286-15-26-S2.mp4]

Funding

This work was supported by Occitania region “Recherche et Société(s)” program in the frame of DIMENSION project N°2018-003267.

ORCID® iDs

Vincent Astié - https://orcid.org/0000-0001-6548-178X
Romain Parret - https://orcid.org/0000-0003-0662-6373
Sylvie Contreras - https://orcid.org/0000-0002-4733-9998
Matthieu Paillet - https://orcid.org/0000-0001-7038-9101

References

1. Novoselov, K. S.; Jiang, D.; Schedin, F.; Booth, T. J.; Khotkevich, V. V.; Morozov, S. V.; Geim, A. K. *Proc. Natl. Acad. Sci. U. S. A.* **2005,** *102,* 10451–10453. doi:10.1073/pnas.0502848102
2. Gibney, E. *Nature* **2015,** *522,* 274–276. doi:10.1038/522274a
3. Lin, Z.; McCreary, A.; Briggs, N.; Subramanian, S.; Zhang, K.; Sun, Y.; Li, X.; Borys, N. J.; Yuan, H.; Fullerton-Shirey, S. K.; Chernikov, A.; Zhao, H.; McDonnell, S.; Lindenberg, A. M.; Xiao, K.; LeRoy, B. J.; Drndić, M.; Hwang, J. C. M.; Park, J.; Chhowalla, M.; Schaak, R. E.; Javey, A.; Hersam, M. C.; Robinson, J.; Terrones, M. *2D Mater.* **2016,** *3,* 042001. doi:10.1088/2053-1583/3/4/042001

4. Withers, F.; Del Pozo-Zamudio, O.; Mishchenko, A.; Rooney, A. P.; Gholinia, A.; Watanabe, K.; Taniguchi, T.; Haigh, S. J.; Geim, A. K.; Tartakovskii, A. I.; Novoselov, K. S. *Nat. Mater.* **2015,** *14,* 301–306. doi:10.1038/nmat4205
5. Jariwala, D.; Sangwan, V. K.; Lauhon, L. J.; Marks, T. J.; Hersam, M. C. *ACS Nano* **2014,** *8,* 1102–1120. doi:10.1021/nn500064s
6. Georgiou, T.; Jalil, R.; Belle, B. D.; Britnell, L.; Gorbachev, R. V.; Morozov, S. V.; Kim, Y.-J.; Gholinia, A.; Haigh, S. J.; Makarovsky, O.; Eaves, L.; Ponomarenko, L. A.; Geim, A. K.; Novoselov, K. S.; Mishchenko, A. *Nat. Nanotechnol.* **2013,** *8,* 100–103. doi:10.1038/nnano.2012.224
7. Wang, H.; Yu, L.; Lee, Y.-H.; Shi, Y.; Hsu, A.; Chin, M. L.; Li, L.-J.; Dubey, M.; Kong, J.; Palacios, T. *Nano Lett.* **2012,** *12,* 4674–4680. doi:10.1021/nl302015v
8. Baugher, B. W. H.; Churchill, H. O. H.; Yang, Y.; Jarillo-Herrero, P. *Nat. Nanotechnol.* **2014,** *9,* 262–267. doi:10.1038/nnano.2014.25
9. Zhang, Y. J.; Oka, T.; Suzuki, R.; Ye, J. T.; Iwasa, Y. *Science* **2014,** *344,* 725–728. doi:10.1126/science.1251329
10. Wang, Q. H.; Kalantar-Zadeh, K.; Kis, A.; Coleman, J. N.; Strano, M. S. *Nat. Nanotechnol.* **2012,** *7,* 699–712. doi:10.1038/nnano.2012.193
11. Calman, E. V.; Fogler, M. M.; Butov, L. V.; Hu, S.; Mishchenko, A.; Geim, A. K. *Nat. Commun.* **2018,** *9,* 1895. doi:10.1038/s41467-018-04293-7
12. Rivera, P.; Schaibley, J. R.; Jones, A. M.; Ross, J. S.; Wu, S.; Aivazian, G.; Klement, P.; Seyler, K.; Clark, G.; Ghimire, N. J.; Yan, J.; Mandrus, D. G.; Yao, W.; Xu, X. *Nat. Commun.* **2015,** *6,* 6242. doi:10.1038/ncomms7242
13. Mak, K. F.; Lee, C.; Hone, J.; Shan, J.; Heinz, T. F. *Phys. Rev. Lett.* **2010,** *105,* 136805. doi:10.1103/physrevlett.105.136805
14. Splendiani, A.; Sun, L.; Zhang, Y.; Li, T.; Kim, J.; Chim, C.-Y.; Galli, G.; Wang, F. *Nano Lett.* **2010,** *10,* 1271–1275. doi:10.1021/nl903868w
15. Huang, S.; Ling, X.; Liang, L.; Kong, J.; Terrones, H.; Meunier, V.; Dresselhaus, M. S. *Nano Lett.* **2014,** *14,* 5500–5508. doi:10.1021/nl5014597
16. Scheuschner, N.; Ochedowski, O.; Kaulitz, A.-M.; Gillen, R.; Schleberger, M.; Maultzsch, J. *Phys. Rev. B* **2014,** *89,* 125406. doi:10.1103/physrevb.89.125406
17. Eda, G.; Yamaguchi, H.; Voiry, D.; Fujita, T.; Chen, M.; Chhowalla, M. *Nano Lett.* **2011,** *11,* 5111–5116. doi:10.1021/nl201874w
18. Ribeiro-Soares, J.; Almeida, R. M.; Barros, E. B.; Araujo, P. T.; Dresselhaus, M. S.; Cançado, L. G.; Jorio, A. *Phys. Rev. B* **2014,** *90,* 115438. doi:10.1103/physrevb.90.115438
19. Wilson, J. A.; Yoffe, A. D. *Adv. Phys.* **1969,** *18,* 193–335. doi:10.1080/00018736900101307
20. Lin, M.-L.; Tan, Q.-H.; Wu, J.-B.; Chen, X.-S.; Wang, J.-H.; Pan, Y.-H.; Zhang, X.; Cong, X.; Zhang, J.; Ji, W.; Hu, P.-A.; Liu, K.-H.; Tan, P.-H. *ACS Nano* **2018,** *12,* 8770–8780. doi:10.1021/acsnano.8b05006
21. Cao, Y.; Fatemi, V.; Fang, S.; Watanabe, K.; Taniguchi, T.; Kaxiras, E.; Jarillo-Herrero, P. *Nature* **2018,** *556,* 43–50. doi:10.1038/nature26160
22. Yankowitz, M.; Chen, S.; Polshyn, H.; Zhang, Y.; Watanabe, K.; Taniguchi, T.; Graf, D.; Young, A. F.; Dean, C. R. *Science* **2019,** *363,* 1059–1064. doi:10.1126/science.aav1910
23. Autere, A.; Jussila, H.; Dai, Y.; Wang, Y.; Lipsanen, H.; Sun, Z. *Adv. Mater. (Weinheim, Ger.)* **2018,** *30,* 1705963. doi:10.1002/adma.201705963
24. Hsu, W.-T.; Zhao, Z.-A.; Li, L.-J.; Chen, C.-H.; Chiu, M.-H.; Chang, P.-S.; Chou, Y.-C.; Chang, W.-H. *ACS Nano* **2014,** *8,* 2951–2958. doi:10.1021/nn500228r
25. Yu, H.; Liu, G.-B.; Tang, J.; Xu, X.; Yao, W. *Sci. Adv.* **2017,** *3,* e1701696. doi:10.1126/sciadv.1701696
26. Zhang, X.; Qiao, X.-F.; Shi, W.; Wu, J.-B.; Jiang, D.-S.; Tan, P.-H. *Chem. Soc. Rev.* **2015,** *44,* 2757–2785. doi:10.1039/c4cs00282b
27. Astié, V.; Wasem-Klein, F.; Makhlouf, H.; Paillet, M.; Huntzinger, J.-R.; Sauvajol, J.-L.; Zahab, A.-A.; Juillaguet, S.; Contreras, S.; Voiry, D.; Landois, P., in press.
28. Li, S.-L.; Miyazaki, H.; Song, H.; Kuramochi, H.; Nakaharai, S.; Tsukagoshi, K. *ACS Nano* **2012,** *6,* 7381–7388. doi:10.1021/nn3025173
29. Lee, C.; Yan, H.; Brus, L. E.; Heinz, T. F.; Hone, J.; Ryu, S. *ACS Nano* **2010,** *4,* 2695–2700. doi:10.1021/nn1003937
30. Molina-Sanchez, A.; Wirtz, L. *Phys. Rev. B* **2011,** *84,* 155413. doi:10.1103/physrevb.84.155413
31. Li, X.-L.; Qiao, X.-F.; Han, W.-P.; Zhang, X.; Tan, Q.-H.; Chen, T.; Tan, P.-H. *Nanotechnology* **2016,** *27,* 145704. doi:10.1088/0957-4484/27/14/145704
32. Zhao, Y.; Luo, X.; Li, H.; Zhang, J.; Araujo, P. T.; Gan, C. K.; Wu, J.; Zhang, H.; Quek, S. Y.; Dresselhaus, M. S.; Xiong, Q. *Nano Lett.* **2013,** *13,* 1007–1015. doi:10.1021/nl304169w
33. Zhang, X.; Han, W. P.; Wu, J. B.; Milana, S.; Lu, Y.; Li, Q. Q.; Ferrari, A. C.; Tan, P. H. *Phys. Rev. B* **2013,** *87,* 115413. doi:10.1103/physrevb.87.115413
34. Lee, J.-U.; Cheong, H. *J. Raman Spectrosc.* **2018,** *49,* 66–75. doi:10.1002/jrs.5200
35. Drapcho, S. G.; Kim, J.; Hong, X.; Jin, C.; Shi, S.; Tongay, S.; Wu, J.; Wang, F. *Phys. Rev. B* **2017,** *95,* 165417. doi:10.1103/physrevb.95.165417
36. Carvalho, B. R.; Malard, L. M.; Alves, J. M.; Fantini, C.; Pimenta, M. A. *Phys. Rev. Lett.* **2016,** *116,* 089904. doi:10.1103/physrevlett.116.089904
37. Nemanich, R. J.; Tsai, C. C.; Connell, G. A. N. *Phys. Rev. Lett.* **1980,** *44,* 273–276. doi:10.1103/physrevlett.44.273
38. Lui, C. H.; Ye, Z.; Ji, C.; Chiu, K.-C.; Chou, C.-T.; Andersen, T. I.; Means-Shively, C.; Anderson, H.; Wu, J.-M.; Kidd, T.; Lee, Y.-H.; He, R. *Phys. Rev. B* **2015,** *91,* 165403. doi:10.1103/physrevb.91.165403
39. Huang, S.; Liang, L.; Ling, X.; Puretzky, A. A.; Geohegan, D. B.; Sumpter, B. G.; Kong, J.; Meunier, V.; Dresselhaus, M. S. *Nano Lett.* **2016,** *16,* 1435–1444. doi:10.1021/acs.nanolett.5b05015
40. Liao, M.; Wei, Z.; Du, L.; Wang, Q.; Tang, J.; Yu, H.; Wu, F.; Zhao, J.; Xu, X.; Han, B.; Liu, K.; Gao, P.; Polcar, T.; Sun, Z.; Shi, D.; Yang, R.; Zhang, G. *Nat. Commun.* **2020,** *11,* 2153. doi:10.1038/s41467-020-16056-4
41. Quan, J.; Linhart, L.; Lin, M.-L.; Lee, D.; Zhu, J.; Wang, C.-Y.; Hsu, W.-T.; Choi, J.; Embley, J.; Young, C.; Taniguchi, T.; Watanabe, K.; Shih, C.-K.; Lai, K.; MacDonald, A. H.; Tan, P.-H.; Libisch, F.; Li, X. *Nat. Mater.* **2021,** *20,* 1100–1105. doi:10.1038/s41563-021-00960-1
42. Tiberj, A.; Rubio-Roy, M.; Paillet, M.; Huntzinger, J.-R.; Landois, P.; Mikolasek, M.; Contreras, S.; Sauvajol, J.-L.; Dujardin, E.; Zahab, A.-A. *Sci. Rep.* **2013,** *3,* 2355. doi:10.1038/srep02355
43. Yan, R.; Simpson, J. R.; Bertolazzi, S.; Brivio, J.; Watson, M.; Wu, X.; Kis, A.; Luo, T.; Hight Walker, A. R.; Xing, H. G. *ACS Nano* **2014,** *8,* 986–993. doi:10.1021/nn405826k
44. Melnikova-Kominkova, Z.; Jurkova, K.; Vales, V.; Drogowska-Horná, K.; Frank, O.; Kalbac, M. *Phys. Chem. Chem. Phys.* **2019,** *21,* 25700–25706. doi:10.1039/c9cp04993b
45. Lee, T.; Choi, J.-H.; Ahn, J.-H.; Yoon, Y.-G.; Rho, H. *Appl. Surf. Sci.* **2022,** *579,* 152208. doi:10.1016/j.apsusc.2021.152208

46. Liu, K.; Zhang, L.; Cao, T.; Jin, C.; Qiu, D.; Zhou, Q.; Zettl, A.; Yang, P.; Louie, S. G.; Wang, F. *Nat. Commun.* **2014,** *5,* 4966. doi:10.1038/ncomms5966
47. Rice, C.; Young, R. J.; Zan, R.; Bangert, U.; Wolverson, D.; Georgiou, T.; Jalil, R.; Novoselov, K. S. *Phys. Rev. B* **2013,** *87,* 081307. doi:10.1103/physrevb.87.081307
48. Li, Z.; Lv, Y.; Ren, L.; Li, J.; Kong, L.; Zeng, Y.; Tao, Q.; Wu, R.; Ma, H.; Zhao, B.; Wang, D.; Dang, W.; Chen, K.; Liao, L.; Duan, X.; Duan, X.; Liu, Y. *Nat. Commun.* **2020,** *11,* 1151. doi:10.1038/s41467-020-15023-3
49. Cortijo-Campos, S.; Prieto, C.; De Andrés, A. *Nanomaterials* **2022,** *12,* 1330. doi:10.3390/nano12081330
50. Liu, Q.; Li, L.; Li, Y.; Gao, Z.; Chen, Z.; Lu, J. *J. Phys. Chem. C* **2012,** *116,* 21556–21562. doi:10.1021/jp307124d
51. Debnath, R.; Maity, I.; Biswas, R.; Raghunathan, V.; Jain, M.; Ghosh, A. *Nanoscale* **2020,** *12,* 17272–17280. doi:10.1039/c9nr09897f
52. Mignuzzi, S.; Pollard, A. J.; Bonini, N.; Brennan, B.; Gilmore, I. S.; Pimenta, M. A.; Richards, D.; Roy, D. *Phys. Rev. B* **2015,** *91,* 195411. doi:10.1103/physrevb.91.195411
53. Zhou, X.; Jin, K.; Cong, X.; Tan, Q.; Li, J.; Liu, D.; Luo, J. *J. Colloid Interface Sci.* **2019,** *538,* 159–164. doi:10.1016/j.jcis.2018.11.032
54. Maino, J. L.; Schouten, R.; Umina, P. *J. Appl. Ecol.* **2021,** *58,* 789–800. doi:10.1111/1365-2664.13812

License and Terms

BEILSTEIN JOURNAL OF NANOTECHNOLOGY

On the mechanism of piezoresistance in nanocrystalline graphite

Sandeep Kumar*[1], Simone Dehm[1] and Ralph Krupke[1,2,3]

Full Research Paper

Open Access

Address:
[1]Institute of Nanotechnology, Karlsruhe Institute of Technology, Kaiserstr. 12, 76131 Karlsruhe, Germany, [2]Institute of Quantum Materials and Technologies, Karlsruhe Institute of Technology, Kaiserstr. 12, 76131 Karlsruhe, Germany and [3]Institute of Materials Science, Technische Universität Darmstadt, 64287 Darmstadt, Germany

Email:
Sandeep Kumar* - sandeep.kumar@kit.edu

* Corresponding author

Keywords:
grain boundary; nanocrystalline graphene; strain sensor; Raman; tunneling and destruction

Beilstein J. Nanotechnol. **2024,** *15,* 376–384.
https://doi.org/10.3762/bjnano.15.34

Received: 23 November 2023
Accepted: 19 March 2024
Published: 08 April 2024

This article is part of the thematic issue "Applications of Raman spectroscopy in the characterization of nanomaterials".

Guest Editor: P. Araujo

Abstract

Strain sensors are sensitive to mechanical deformations and enable the detection of strain also within integrated electronics. For flexible displays, the use of a seamlessly integrated strain sensor would be beneficial, and graphene is already in use as a transparent and flexible conductor. However, graphene intrinsically lacks a strong response, and only by engineering defects, such as grain boundaries, one can induce piezoresistivity. Nanocrystalline graphene (NCG), a derivative form of graphene, exhibits a high density of defects in the form of grain boundaries. It holds an advantage over graphene in easily achieving wafer-scale growth with controlled thickness. In this study, we explore the piezoresistivity in thin films of nanocrystalline graphite. Simultaneous measurements of sheet resistance and externally applied strain on NCG placed on polyethylene terephthalate (PET) substrates provide intriguing insights into the underlying mechanism. Raman measurements, in conjunction with strain applied to NCG grown on flexible glass, indicate that the strain is concentrated at the grain boundaries for smaller strain values. For larger strains, mechanisms such as grain rotation and the formation of nanocracks might contribute to the piezoresistive behavior in nanocrystalline graphene.

Introduction

Flexible strain sensors are an important factor in moving from rigid to flexible electronics. Graphene, because of its interesting inherent properties, has found its way in many applications [1-3]. In particular, it is a promising alternative material as a transparent and conductive coating for future flexible electronics. This is because the relative change in resistance of graphene for similar values of applied strain (4%) is just 50%, which is two orders of magnitude lower than that of the flat-screen material indium titanium oxide (ITO). Indeed, from a theoretical point of view, change in resistance due to strain or piezoresistivity in graphene is expected to be small because the displacement of the Dirac point occurs in continuous k space, and strain-induced lattice distortions do not change the local band structure up to 20% strain [4]. In contrast, because of the

quantized *k* space in carbon nanotubes, uniaxial strain can induce band opening or closing. Nevertheless, strain-induced resistance modulation in graphene is by far not zero, and reported values for relative resistance changes vary between 0.1% and 50% at 3% strain [5-8]. Although several works report the enhancement of piezoresistance in graphene, it is still unclear which factors influence this property. A theoretical work by Kumar et al. suggested that grain boundaries can affect piezoresistance in graphene [9]. This result seemed unexpected since Dirac particles should undergo Klein tunneling at barriers without adding up to the total resistance. However, the theoretical modeling shows that the modulation of the transport gap under strain is sensitive to the degree of asymmetry of the grain boundaries. While the symmetric grain boundaries remain metallic in the presence of uniaxial strain, the transport gap of the asymmetric semiconducting grain boundaries can be considerably increased in the presence of strain. Hence, the asymmetric metallic grain boundaries undergo a metal–semiconductor transition in the presence of strain. This effect could open a way to utilize grain boundaries in graphene for fabricating highly sensitive transparent strain sensors.

So far, the growth of specific grain boundaries in graphene has not been reported. Also, most research activities aim at the chemical vapor deposition (CVD) synthesis of monocrystalline graphene free of grain boundaries [10-12]. Methods to detect and visualize grain boundaries and dislocations are currently under development [13,14]. This leads to the situation that the role of grain boundaries for graphene-based sensing of strain, pressure, and motion has not been explored and remains unresolved [15-18], although in CVD graphene the domain size is typically of the order of a few micrometers [11]. We speculated that if grain boundaries are responsible for piezoresistivity in graphene, then the gauge factor should be enhanced if one reduces the grain size to a few nanometers.

Nanocrystalline graphene (NCG) is graphitic material with a crystal size of nanometers and, therefore, an excellent candidate for piezoresistance devices. Also, wafer-scale synthesis of NCG has already been achieved by Zhang et al. and modified by Riaz and co-workers [19,20]. Thickness-controlled growth of NCG was exploited to utilize it as an efficient broadband photodetector [21,22]. The preliminary work on the piezoresistivity of NCG looked promising but was limited regarding the applied strain because of rigid SiO_2/Si substrates. In this work, we focus on the piezoresistance measurements in NCG at larger strain values. Initially, a two-point bending setup is described, which was constructed in-house and automated using Python. Then, sheet resistance measurements under externally applied strain are discussed. Raman spectroscopy of the NCG under strain is studied, which gives insights into the distribution of strain in the film. Utilizing electrical and optical properties, a mechanism for piezoresistance in NCG is proposed. The work included here is a part of the PhD thesis completed by the first author S. Kumar [23].

Results and Discussion

The two-point bending fixture, which was constructed to impart external strain and simultaneously perform sheet resistance measurements and Raman spectroscopy, is shown in Figure 1a.

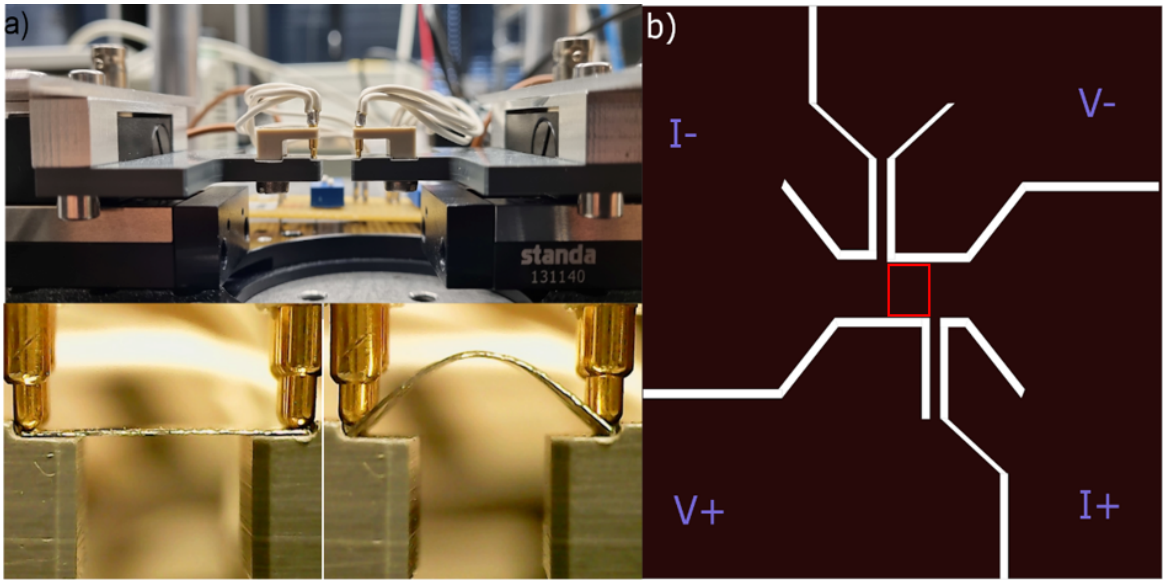

Figure 1: (a) Two-point bending fixture showing two instances of a substrate during measurement. (b) Patterned NCG structure for piezoresistance measurements. The red square marks the active device area. White lines are regions where NCG has been etched.

Two instances of zero and non-zero strain are also depicted. The setup has two stepper motors acquired from Standa Inc. The contacts on the NCG were made by gold-coated spring pressure contacts, which were then connected to a BNC connector and a Keithley 2636A device. The substrate holder and contacts holder were machined and attached to the stepper motor as shown in Figure 1a. A detailed description of the setup has been given by Kumar [23]. The complete setup was automated via self-programmed Python code. To completely eliminate any strain-induced changes in the contacts, the NCG was patterned such that the NCG itself is used as a contacting electrode (shown in Figure 1b). The area marked with a red square in Figure 1b (2 mm × 2 mm) is the active device area for sheet resistance measurements on a substrate of 10 mm × 10 mm area. Thin NCG constrictions at the end of the active device area were used to measure the potential drop across the device area. The measurements were done in constant current mode, and the voltage drop across the squared central area was measured at each strain value.

NCG was grown by spin coating S1805 at 4000 rpm; subsequently, it was transferred onto a 100 µm thick PET substrate. For more details please see the Experimental section. Measured piezoresistance curves (with forward and reverse sweep) for a 5 nm thick patterned NCG film on the PET substrate are shown in Figure 2a. Sheet resistance values are plotted against tensile

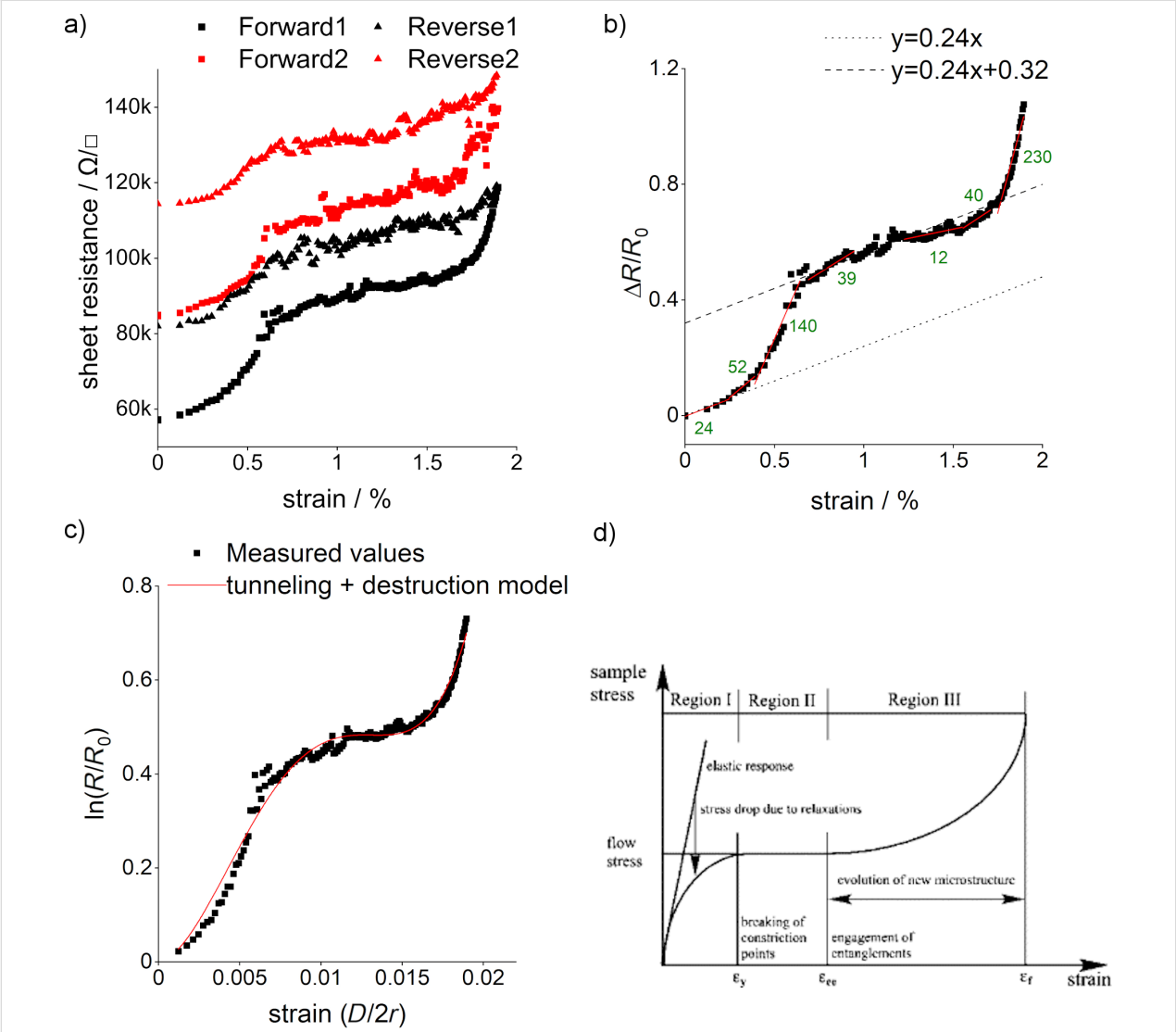

Figure 2: (a) Sheet resistance vs strain curve for NCG shown for two subsequently measured cycles of bending. (b) $\Delta R/R_0$ specifying GFs. The two parallel lines indicate similar GFs in two strain regimes. (c) Logarithm of normalized resistance vs strain curve for NCG with tunneling and destruction model [24]. (d) Typical stress–strain curve of amorphous polymer PMMA film (reprinted from [32], Polymer, Vol. 44, Issue 19, by Z. H. Stachurski, "Strength and deformation of rigid polymers: the stress–strain curve in amorphous PMMA", pages 6067–6076, Copyright (2003), with permission from Elsevier. This content is not subject to CC BY 4.0.)

strain up to 2%, which is an order of magnitude larger than in our previous work (max 0.1%) [19]. We could reproduce the previously observed gauge factor (GF) of ca. 24 at very low strain where the sheet resistance increases linearly with strain (<0.3%); however, in the extended-strain region we observe now a super-linear behavior, which evolves into a linear region from 0.7% to 1.6% strain, before entering a super-linear regime beyond 1.6% strain. The GF values from the the plot of normalized change in resistance vs strain (Figure 2b) also depict how the rate of resistance change with strain drops and then increases again. Interestingly, the GF is similar below 0.3% and in the region between 0.7% and 1.6% strain, indicating a similar origin of piezoresistance (shown by two parallel lines in Figure 2b). The overall shape of the curves is reproducible and shown here for two strain cycles. However, a hysteresis is observed between forward and reverse sweeps, indicating that structural changes in the films occur, which are in part irreversible.

To gain insights into the strain distribution in the strained NCG, we performed in situ Raman measurements with strain as shown in Figure 3a. The flexible glass was preferred for the Raman measurements because the spectra of NCG cannot be resolved on PET as a result of a strong Raman signal of the substrate itself. The 50 µm thick flexible glass was acquired from Schott. The glass loses its flexibility at 600 °C and also in water [23]. To keep the flexibility, the NCG film was grown on both sides of the glass substrate. There are three reasons for that. First, the negative thermal expansion coefficient of NCG prevents the release of stress initially present in the glass [25]. Second, the film protects the glass from any corrosion from water if the transfer is required on glass in an aqueous medium

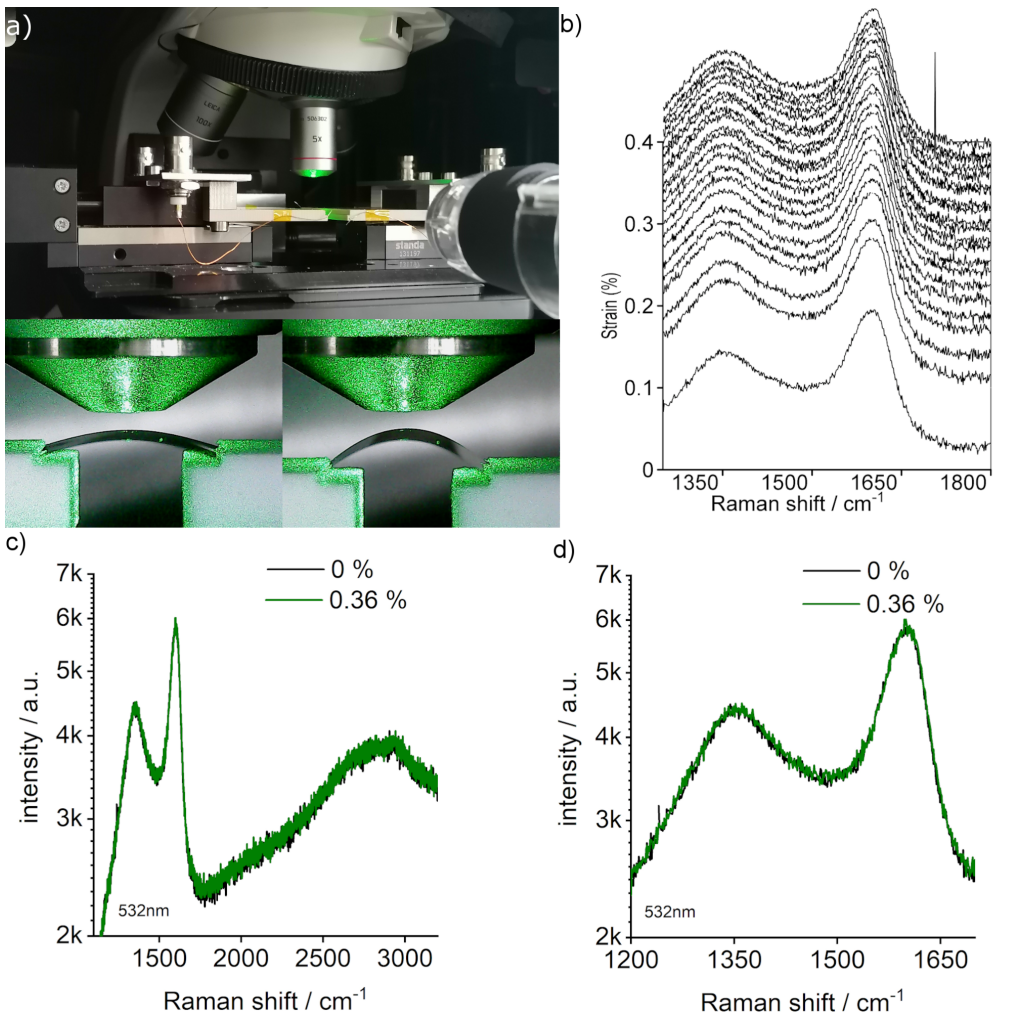

Figure 3: (a) Piezoresistance measurement setup enabling in situ Raman measurements under strain. (b) Raman spectra of NCG on glass with increasing strain from 0% (bottom) to 0.36% (top). Curves were shifted for clarity. (c) Comparison of full-range Raman spectra for 0% (black) and 0.36% (green) strain. (d) Comparison of Raman spectra focused on D and G peaks for 0% (black) and 0.36% (green) curves.

[26]. Third, NCG fills the cracks present at the edges during spin coating the polymer and inhibits their propagation during the bending of the substrate.

Raman spectroscopy is a powerful method to detect strain in graphene, which can be determined from the analysis of the peak position of the 2D and G modes [27]. For the Raman measurements, the bending setup was installed in a Renishaw inVia Raman microscope, operated at 532 nm excitation wavelength (Figure 3a) with a 100× objective. Concado et al. [28] reported the general equation for calculating the crystallite size based on the full width at half maximum (FWHM) and intensity ratios of D and G peaks. Similar to our previous work [19], we use the FWHM of D and G peaks here at zero strain to calculate the crystallite size. The G peak gives a crystallite size of 2–3 nm, and the D peak corresponds to a crystallite size of 4–5 nm. TEM studies also done in our previous work on NCG gave an average domain size of 3 nm. We therefore report a grain size range of 2–5 nm for the NCG film synthesized for this study.

Figure 3b shows the Raman spectra as a waterfall plot for strain values up to 0.36%. Figure 3c,d shows a comparison between the spectra taken at 0% and 0.36% strain. Further measurements with increased strain could not be taken due to the failure of the glass substrate. Interestingly, no prominent changes in peak positions, widths, or intensity could be detected, inferring that the strain within the grains remains constant even though the externally applied strain increased to ca. 0.4%.

In an attempt to model piezoresistance in NCG, we have used the tunneling + destruction model for composite materials [24]:

$$\ln\frac{R}{R_0} = \ln(1+\varepsilon) + \alpha\varepsilon + \beta\varepsilon^2 + \gamma\varepsilon^3 + \delta\varepsilon^4.$$

The model with five free parameters was fitted to the data as shown in Figure 2c, and the fit parameters are given in Table 1. The model was initially given for a matrix in which conducting particles are dispersed in a polymer matrix and are separated by tunnel junctions. In this model, the conductivity in the film is determined by the number of conductive paths, N, and the tunneling distance, d. The model has been used to explain the piezoresistance for several composite materials [29,30].

Zhao et al. [24] used the model to explain the piezoresistance in nanographene films, although the material is comparable to ours and not a composite material in the original sense. NCG can be considered as a matrix of grains and grain boundaries (GBs), where the grains are separated by the GBs and have different resistivities [31]. Hence, the tunneling + destruction model might indeed be an appropriate physical representation of the nano/microstructure of NCG. The model explains that at lower strain values, only the tunneling distance d increases, but N remains constant. Whereas at larger strain values, d and N both change; therefore, the GF increases at those values. Our Raman measurements indicate that at least up to 0.4% strain, no strain is experienced by the grains, which would mean that all the strain energy provided externally ends up at GBs leading to movements of dislocations at GBs or fractures at GBs. Fitting the tunneling + destruction model to our data, we find that the initial tunneling distance has a value of 3.6 nm, which is comparable to the nanographene films fabricated by Zhao et al. (3.4 nm) [24]. The destruction of conduction channels as part of the tunneling + destruction model then takes place at higher strain values and eventually leads to partial irreversibility, which can be observed as an offset between the first and second trace in Figure 2a. Nevertheless, the overall shape of the second curve is similar to the first one. Figure 2d shows a typical stress vs strain curve for a polymer film [32]. The trend of the curve looks similar to the resistance vs strain curve for NCG in Figure 2a. Since polymers are insulators, literature on resistance vs strain for such films does not exist. However, it depicts how the stress drops because of strain relaxation in such films. Since resistance is directly proportional to strain in the tunneling + destruction model, one can think that the resistance of such films would also drop. Based on strain relaxations, therefore, one can correlate NCG and a polymer material and potentially give insight into how NCG behaves in the plateau region of the resistance vs strain curve.

Table 1: Value of extracted parameters by fitting from Figure 2c.

Parameter	Value
α	5
β	$1.55 \times 10^4 \pm 1.8 \times 10^2$
γ	$-1.63 \times 10^6 \pm 2.5 \times 10^4$
δ	$4.6 \times 10^7 \pm 8.6 \times 10^5$

It is important to note that many works that have reported piezoresistance in NCG have recorded data at comparably low strain values and have not observed the plateau-like region as reported here, where the gauge factor is similar to the gauge factor at very low strain [24,33]. A plateau-like region has neither been observed in nanocrystalline graphite [33], amorphous carbon films [34], nor in metallic films [35]. The mechanism that leads to an increase of resistance in amorphous carbon and gold films at large strain is crack formation. Also, in NCG, which is full of GBs and defects, crack formation and propagation have to be considered [36]. Assuming nanocrack formation at the GBs, we could understand the entire piezoresistance curve in the following way. The increase in resistance at

lower strain (0.3%) would be determined by the piezoresistance of the GBs, as studied by Kumar and co-workers [9]. Beyond this strain value, the resistance of the film increases rapidly, which can be understood by nanocrack formation at certain GBs [37]. This phenomenon occurs up to 0.7% strain and then stops. The reason could be that the remaining GBs are stronger than the ones that fractured between 0.3% and 0.7% strain. The plateau after 0.7% strain indicates that although the strain is increased, no crack formation occurs. In addition, the slopes of the resistance vs strain curve at smaller strain and the plateau region are similar (Figure 2b), indicating a similar piezoresistance mechanism in both strain regions. This can be understood by strain relaxation occurring at GBs by crack formation and bond movement, as well as reformation and changes in the microstructure of the film [37]. After the plateau (strain > 1.6%), the resistance once again increases, and a new set of nanocracks start to form at different GBs. The second cycle of the resistance vs strain measurement (Figure 2a, red curve) starts from a resistance value that is equivalent to the resistance at 0.7% strain in the first cycle. This indicates that the nanocracks formed in the NCG film between 0.3% to 0.7% strain are non-reversible cracks. However, the cracks formed between 1.6% and 2.0% strain are partially reversible, and the resistance values are almost recovered. This is possible through bond reformations by formation of pentagon–heptagon pairs due to their low formation energy [38,39]. In addition, the formation of nanocracks appears not so pronounced in the second cycle, as can be seen from the change in resistance between 0.3% and 0.7% and between 1.6% and 2.0% strain, and is likely due to cracks already formed in the first cycle.

Another process that might be considered for strain relaxation is grain rotation as shown in Figure 4. The rotation of grains during the straining of metal films has been studied extensively [40,41]. The effect is prominent for metal films with smaller grain sizes and diminishes with larger grains. The mechanism has been proposed as a cause of plastic deformation in metals. Wang et al. showed for a platinum nanocrystalline film [42] that the rotation due to strain at room temperature does not occur because of cross-grain gliding, GB sliding, or diffusional creep processes. The rotation occurs because of a change in the content of GB dislocations, which can change the GB angle between the grains (Frank–Bilby equation).

We cannot completely exclude that GB rotation occurs to some extent also in strained nanocrystalline graphene. Figure 4 shows a schematic of a NCG film under strain correlated with the transport of the film. The black dots represent the grain position, and the arrows represent the long axis of non-spherical grains. At the beginning, marked as point A on the curve, the grains are randomly oriented. As the strain is applied, the grains start to move apart, which is visible as an increase in resistance values between 0% and 0.3% strain [24], also confirmed by Raman measurements under strain (Figure 3b–d). At 0.3% to

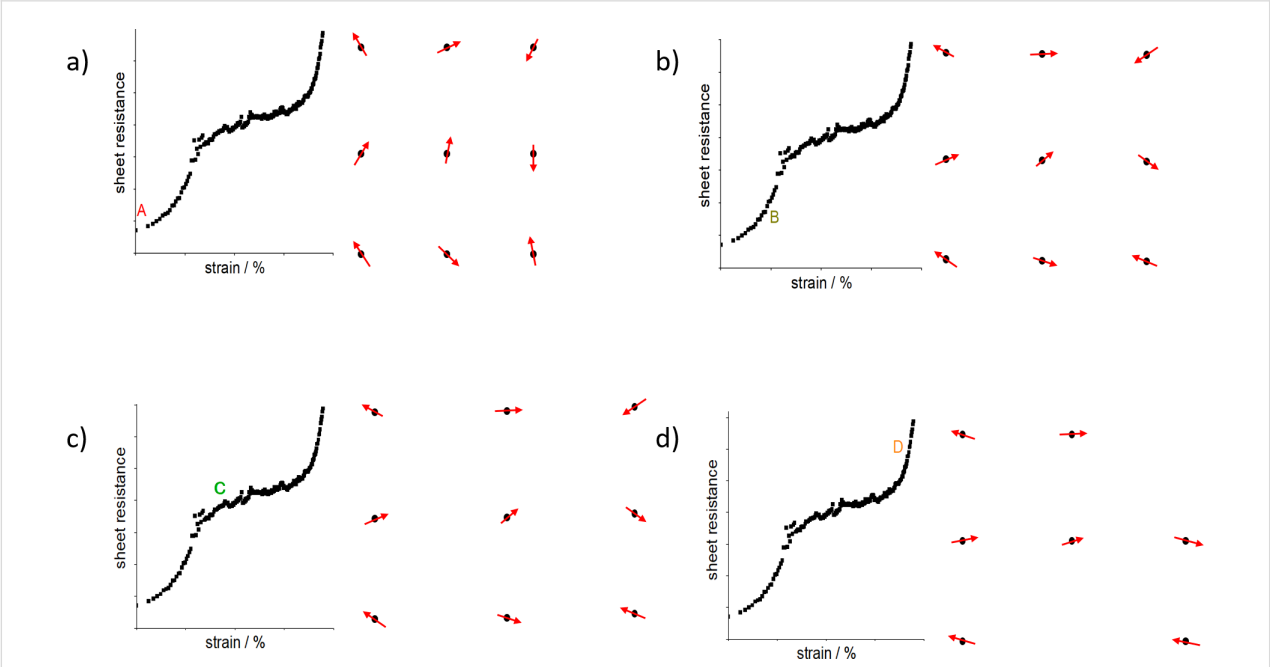

Figure 4: Correlation between transport in NCG films and grain rotation and reorientation under strain. Black dots represent the grain position, and arrows represent the long axis of non-spherical grains (a) at zero strain (marked as point A in the curve), (b) at point B in the curve, (c) in the plateau region marked as point C, and (d) at point D in the curve showing missing grains as rupture in the film.

0.7% strain, grain rotation and irreversible changes in the microstructure occur. This is seen by a sharper increase in resistance and a larger GF value, which corresponds to point B in Figure 4b showing grains moving apart in combination with grain rotation. At the plateau region (0.7%–1.6%), as explained before, the slope of the resistance vs strain curve is equivalent to the lower strain region (0%–0.3%) indicating a similar piezoresistance mechanism of grains moving apart and increasing tunneling distance. This is shown as point C in the transport in Figure 4c, where the grains are locked and cannot rotate, and the increase in resistance only occurs because of increased distance between grains. Above 1.6% strain, a sharper increase in resistance indicates again grain rotation and reorientation, and fracture in the film shown by missing black dots and arrows in Figure 4d, corresponding to point D in the transport curve. The processes of grain movements (increase in distance between grains and rotation) would repeat if the strain values are increased further until the fracture of the film. The process of bond rotation and reformation is known in NCG films for the relaxation of stress at GBs [37]. When the application of strain is reversed, irreversible changes occurring in the film by grain rotation results in a permanent increase in initial resistance seen by a hysteresis (blach and red curves in Figure 2a) and an offset in the second cycle (red curve in Figure 2a) [43]. Although the processes are different, there is a competition between bond breaking and rotation at certain strain values; the kinetically favorable process occurs in alternating sequences related to thermal and stress fluctuations inducing nanocrack formation [37,44]. Yang et al. [45] have shown a simulation of the stress vs strain behavior in NCG films at different temperatures and strain rates. Interestingly, the curve looks similar to the resistance vs strain curve in this work. A deviation from the linear behavior into a plateau is observed at larger strain, owing to plastic deformations of the NCG film. However, a sharp increase in stress after the plateau region is not observed. This can be understood by stress relaxation due to fractures in the film at higher strain, which is visible in resistance vs strain curves as a sharp increase in the resistance. As a last comment, Zhao et al. [24] reported that as they reduced the grain size from 25 to 8 nm, the GF increased from 11 to 600. Also, Simionescu et al. [33] reported a varying GF (50–250) for a strain range of 0%–1%. In this work, NCG with lower grain sizes has been obtained; however, the GF does not appear to further increase and remains comparable to the values of previously reported works. A comparison is tabulated in Table 2.

Table 2: Comparison of grain sizes of NCG with the corresponding GFs.

Grain size (nm)	Gauge factor (GF)	Strain range (%)	Reference
25	11	0 to 1	[24]
8	600	0 to 1	[24]
9	50–250	0 to 1	[33]
2–5	23	0 to 0.1	[19]
2–5	24–140	0 to 2	this work

Conclusion

This study endeavors to further the understanding of the piezoresistance mechanism in NCG, employing a two-point bending setup to apply controlled strain. The strained NCG was analyzed electrically and optically, revealing three regimes in the sheet resistance vs strain curve. Examination of the results from optical and electrical measurements suggests that in the lower strain regime, the grains experience negligible effects, while the majority of strain is concentrated at the grain boundaries. Consequently, non-reversible cracks form at GBs. The second regime exhibits a superlinear dependence of sheet resistance on strain, indicating potential grain rotation and bond reformation, leading to a modified nano/microstructure. In the larger-strain regime, an exponential increase in sheet resistance vs strain signifies further partially reversible crack formation. To enhance understanding, a tunneling + destruction model was fitted, and parameters were extracted. While the paper offers an overview of piezoresistance in NCG, a more in-depth study is imperative for a complete comprehension of the system's complexity. In situ FTIR measurements could provide additional insights into changes in doping and defects with strain.

Experimental

Piezoresistance measurements

NCG was synthesized on a 300 nm SiO_2/Si substrate by spin coating S1805 (1:10 dilution with propylene glycol methyl ether acetate, PGMEA) at 4000 rpm. The spin-coated Si/SiO_2 substrate was loaded in a vacuum furnace and annealed at 600 °C for 10 h at 10^{-6} mbar. The measured thickness of the grown film was ca. 5 nm. The NCG film was then transferred onto a 100 µm thick PET substrate. For the transfer process, first, the NCG film on SiO_2/Si was coated with 200 nm thick PMMA and put into 5 M NaOH solution at 80 °C. The NCG/PMMA film floats on the surface after the etching of SiO_2. Using a clean glass wafer, the NCG/PMMA film was transferred from the NaOH solution to a clean water beaker and allowed to float on the top. The cleaning was repeated three times to ensure the no residues of NaOH remained on the NCG film. The film was then removed from the water using a PET substrate. After that, the substrate was left in air for drying. Next, a drop of PMMA was dripped on top of the film and allowed to spread and dry. This has been shown to be helpful in removing wrinkles formed during the transfer process [46]. The NCG film on the PET substrate was then patterned in the structure shown in Figure 1b

using e-beam lithography. There were no metal films deposited on NCG, and the electrical contact was made between gold spring contacts and NCG directly. For Raman measurements, S1805 (1:10 dilution with PGMEA) was spin-coated on both sides of the flexible glass substrate at 4000 rpm to grow NCG on both sides of the glass. The substrate was then loaded into the vacuum furnace and treated similarly.

Raman measurements

Raman measurements were done using a 100× objective at 0.6 mW laser power for 60 s integration time for each measurement. The same area on the NCG film was focused as to monitor and compare any changes occurring during straining the film.

ORCID® iDs

Sandeep Kumar - https://orcid.org/0000-0003-0991-9438
Simone Dehm - https://orcid.org/0000-0002-3431-4732
Ralph Krupke - https://orcid.org/0000-0001-8427-8592

References

1. Choi, J. H.; Lee, J.; Byeon, M.; Hong, T. E.; Park, H.; Lee, C. Y. *ACS Appl. Nano Mater.* **2020,** *3,* 2257–2265. doi:10.1021/acsanm.9b02378
2. Fu, W.; Nef, C.; Knopfmacher, O.; Tarasov, A.; Weiss, M.; Calame, M.; Schönenberger, C. *Nano Lett.* **2011,** *11,* 3597–3600. doi:10.1021/nl201332c
3. Yavari, F.; Castillo, E.; Gullapalli, H.; Ajayan, P. M.; Koratkar, N. *Appl. Phys. Lett.* **2012,** *100,* 203120. doi:10.1063/1.4720074
4. Pereira, V. M.; Castro Neto, A. H.; Peres, N. M. R. *Phys. Rev. B* **2009,** *80,* 045401. doi:10.1103/physrevb.80.045401
5. Bae, S.; Kim, H.; Lee, Y.; Xu, X.; Park, J.-S.; Zheng, Y.; Balakrishnan, J.; Lei, T.; Ri Kim, H.; Song, Y. I.; Kim, Y.-J.; Kim, K. S.; Özyilmaz, B.; Ahn, J.-H.; Hong, B. H.; Iijima, S. *Nat. Nanotechnol.* **2010,** *5,* 574–578. doi:10.1038/nnano.2010.132
6. Bae, S.-H.; Lee, Y.; Sharma, B. K.; Lee, H.-J.; Kim, J.-H.; Ahn, J.-H. *Carbon* **2013,** *51,* 236–242. doi:10.1016/j.carbon.2012.08.048
7. Fu, X.-W.; Liao, Z.-M.; Zhou, J.-X.; Zhou, Y.-B.; Wu, H.-C.; Zhang, R.; Jing, G.; Xu, J.; Wu, X.; Guo, W.; Yu, D. *Appl. Phys. Lett.* **2011,** *99,* 213107. doi:10.1063/1.3663969
8. Li, X.; Zhang, R.; Yu, W.; Wang, K.; Wei, J.; Wu, D.; Cao, A.; Li, Z.; Cheng, Y.; Zheng, Q.; Ruoff, R. S.; Zhu, H. *Sci. Rep.* **2012,** *2,* 870. doi:10.1038/srep00870
9. Kumar, S. B.; Guo, J. *Nano Lett.* **2012,** *12,* 1362–1366. doi:10.1021/nl203968j
10. Lee, J.-H.; Lee, E. K.; Joo, W.-J.; Jang, Y.; Kim, B.-S.; Lim, J. Y.; Choi, S.-H.; Ahn, S. J.; Ahn, J. R.; Park, M.-H.; Yang, C.-W.; Choi, B. L.; Hwang, S.-W.; Whang, D. *Science* **2014,** *344,* 286–289. doi:10.1126/science.1252268
11. Bonaccorso, F.; Lombardo, A.; Hasan, T.; Sun, Z.; Colombo, L.; Ferrari, A. C. *Mater. Today* **2012,** *15,* 564–589. doi:10.1016/s1369-7021(13)70014-2
12. Li, X.; Magnuson, C. W.; Venugopal, A.; Tromp, R. M.; Hannon, J. B.; Vogel, E. M.; Colombo, L.; Ruoff, R. S. *J. Am. Chem. Soc.* **2011,** *133,* 2816–2819. doi:10.1021/ja109793s
13. Butz, B.; Dolle, C.; Niekiel, F.; Weber, K.; Waldmann, D.; Weber, H. B.; Meyer, B.; Spiecker, E. *Nature* **2014,** *505,* 533–537. doi:10.1038/nature12780
14. Duong, D. L.; Han, G. H.; Lee, S. M.; Gunes, F.; Kim, E. S.; Kim, S. T.; Kim, H.; Ta, Q. H.; So, K. P.; Yoon, S. J.; Chae, S. J.; Jo, Y. W.; Park, M. H.; Chae, S. H.; Lim, S. C.; Choi, J. Y.; Lee, Y. H. *Nature* **2012,** *490,* 235–239. doi:10.1038/nature11562
15. Smith, A. D.; Niklaus, F.; Paussa, A.; Vaziri, S.; Fischer, A. C.; Sterner, M.; Forsberg, F.; Delin, A.; Esseni, D.; Palestri, P.; Östling, M.; Lemme, M. C. *Nano Lett.* **2013,** *13,* 3237–3242. doi:10.1021/nl401352k
16. Zhu, S.-E.; Krishna Ghatkesar, M.; Zhang, C.; Janssen, G. C. A. M. *Appl. Phys. Lett.* **2013,** *102,* 161904. doi:10.1063/1.4802799
17. Hosseinzadegan, H.; Todd, C.; Lal, A.; Pandey, M.; Levendorf, M.; Park, J. Graphene has ultra high piezoresistive gauge factor. In *2012 IEEE 25th International Conference on Micro Electro Mechanical Systems (MEMS),* Paris, France, Jan 29–Feb 2, 2012; IEEE; pp 611–614. doi:10.1109/memsys.2012.6170262
18. Smith, A. D.; Vaziri, S.; Niklaus, F.; Fischer, A. C.; Sterner, M.; Delin, A.; Östling, M.; Lemme, M. C. *Solid-State Electron.* **2013,** *88,* 89–94. doi:10.1016/j.sse.2013.04.019
19. Riaz, A.; Pyatkov, F.; Alam, A.; Dehm, S.; Felten, A.; Chakravadhanula, V. S. K.; Flavel, B. S.; Kübel, C.; Lemmer, U.; Krupke, R. *Nanotechnology* **2015,** *26,* 325202. doi:10.1088/0957-4484/26/32/325202
20. Zhang, Z.; Ge, B.; Guo, Y.; Tang, D.; Wang, X.; Wang, F. *Chem. Commun.* **2013,** *49,* 2789–2791. doi:10.1039/c3cc00089c
21. Peyyety, N. A.; Kumar, S.; Li, M.-K.; Dehm, S.; Krupke, R. *ACS Appl. Mater. Interfaces* **2022,** *14,* 9525–9534. doi:10.1021/acsami.1c24306
22. Parmar, D.; Dehm, S.; Peyyety, N. A.; Kumar, S.; Krupke, R. *Adv. Sens. Res.* **2024,** *3,* 2300134. doi:10.1002/adsr.202300134
23. Kumar, S. *Nanocarbon Devices and Sensors*. Ph.D. Thesis, TU Darmstadt, Germany, 2022. doi:10.26083/tuprints-00021384
24. Zhao, J.; Wang, G.; Yang, R.; Lu, X.; Cheng, M.; He, C.; Xie, G.; Meng, J.; Shi, D.; Zhang, G. *ACS Nano* **2015,** *9,* 1622–1629. doi:10.1021/nn506341u
25. Yoon, D.; Son, Y.-W.; Cheong, H. *Nano Lett.* **2011,** *11,* 3227–3231. doi:10.1021/nl201488g
26. Singh Raman, R. K.; Tiwari, A. *JOM* **2014,** *66,* 637–642. doi:10.1007/s11837-014-0921-3
27. Lee, J. E.; Ahn, G.; Shim, J.; Lee, Y. S.; Ryu, S. *Nat. Commun.* **2012,** *3,* 1024. doi:10.1038/ncomms2022
28. Cançado, L. G.; Takai, K.; Enoki, T.; Endo, M.; Kim, Y. A.; Mizusaki, H.; Jorio, A.; Coelho, L. N.; Magalhães-Paniago, R.; Pimenta, M. A. *Appl. Phys. Lett.* **2006,** *88,* 163106. doi:10.1063/1.2196057
29. Al-solamy, F. R.; Al-Ghamdi, A. A.; Mahmoud, W. E. *Polym. Adv. Technol.* **2012,** *23,* 478–482. doi:10.1002/pat.1902
30. Zhang, X.-W.; Pan, Y.; Zheng, Q.; Yi, X.-S. *J. Polym. Sci., Part B: Polym. Phys.* **2000,** *38,* 2739–2749. doi:10.1002/1099-0488(20001101)38:21<2739::aid-polb40>3.0.co;2-o
31. Zhao, T.; Xu, C.; Ma, W.; Liu, Z.; Zhou, T.; Liu, Z.; Feng, S.; Zhu, M.; Kang, N.; Sun, D.-M.; Cheng, H.-M.; Ren, W. *Nat. Commun.* **2019,** *10,* 4854. doi:10.1038/s41467-019-12662-z
32. Stachurski, Z. H. *Polymer* **2003,** *44,* 6067–6076. doi:10.1016/s0032-3861(03)00554-8
33. Simionescu, O.-G.; Pachiu, C.; Ionescu, O.; Dumbrăvescu, N.; Buiu, O.; Popa, R. C.; Avram, A.; Dinescu, G. *Rev. Adv. Mater. Sci.* **2020,** *59,* 306–313. doi:10.1515/rams-2020-0031
34. Leterrier, Y.; Pinyol, A.; Rougier, L.; Waller, J. H.; Månson, J.-A. E. *J. Appl. Phys.* **2009,** *106,* 113508. doi:10.1063/1.3266001

35. Cho, C.; Kang, P.; Taqieddin, A.; Jing, Y.; Yong, K.; Kim, J. M.; Haque, M. F.; Aluru, N. R.; Nam, S. *Nat. Electron.* **2021,** *4,* 126–133. doi:10.1038/s41928-021-00538-4
36. Shekhawat, A.; Ritchie, R. O. *Nat. Commun.* **2016,** *7,* 10546. doi:10.1038/ncomms10546
37. Yang, Z.; Huang, Y.; Ma, F.; Sun, Y.; Xu, K.; Chu, P. K. *Mater. Sci. Eng., B* **2015,** *198,* 95–101. doi:10.1016/j.mseb.2015.03.019
38. Yazyev, O. V. *Solid State Commun.* **2012,** *152,* 1431–1436. doi:10.1016/j.ssc.2012.04.045
39. Malola, S.; Häkkinen, H.; Koskinen, P. *Phys. Rev. B* **2010,** *81,* 165447. doi:10.1103/physrevb.81.165447
40. Argon, A. S.; Yip, S. *Philos. Mag. Lett.* **2006,** *86,* 713–720. doi:10.1080/09500830600986091
41. Yamakov, V.; Wolf, D.; Phillpot, S. R.; Mukherjee, A. K.; Gleiter, H. *Nat. Mater.* **2004,** *3,* 43–47. doi:10.1038/nmat1035
42. Wang, L.; Teng, J.; Liu, P.; Hirata, A.; Ma, E.; Zhang, Z.; Chen, M.; Han, X. *Nat. Commun.* **2014,** *5,* 4402. doi:10.1038/ncomms5402
43. Yang, Z.; Huang, Y.; Ma, F.; Miao, Y.; Bao, H.; Xu, K.; Chu, P. K. *RSC Adv.* **2016,** *6,* 60856–60861. doi:10.1039/c6ra05167g
44. Ovid'ko, I. A.; Sheinerman, A. G. *J. Phys. D: Appl. Phys.* **2013,** *46,* 345305. doi:10.1088/0022-3727/46/34/345305
45. Yang, Z.; Huang, Y.; Ma, F.; Sun, Y.; Xu, K.; Chu, P. K. *Eur. Phys. J. B* **2015,** *88,* 135. doi:10.1140/epjb/e2015-50850-x
46. Li, X.; Zhu, Y.; Cai, W.; Borysiak, M.; Han, B.; Chen, D.; Piner, R. D.; Colombo, L.; Ruoff, R. S. *Nano Lett.* **2009,** *9,* 4359–4363. doi:10.1021/nl902623y

License and Terms